PROPERTIES OF $La_{2-x}Sr_xCuO_4$ UNDER EPITAXIAL STRAIN: PHOTOEMISSION ON ULTRA THIN FILMS GROWN BY PULSED LASER DEPOSITION

THÈSE N^{O} 3333 (2005)

PRÉSENTÉE À LA FACULTÉ SCIENCES DE BASE

Institut de physique de la matière complexe

SECTION DE PHYSIQUE

ÉCOLE POLYTECHNIQUE FÉDÉRALE DE LAUSANNE

POUR L'OBTENTION DU GRADE DE DOCTEUR ÈS SCIENCES

PAR

Dominique CLOËTTA

ingénieur physicien diplômé EPF
de nationalité suisse et originaire de Zurich (ZH)

acceptée sur proposition du jury:

Prof. D. Pavuna, directeur de thèse
Prof. A. Gauzzi, rapporteur
Prof. H. Keller, rapporteur
Prof. H. J. Mathieu, rapporteur

Lausanne, EPFL
2005

Table of Contents

Abstract

The subject of this thesis is the growth and analysis of high temperature superconductor (HTSC) films and the study of their electronic structure and properties. In particular, the effect of epitaxial strain is investigated, predominantly by means of in-situ angle resolved photoemission spectroscopy (ARPES), as well as X-ray diffraction, resistivity and susceptibility measurements.

In order to achieve that goal we have developed a unique experimental set-up at the Synchrotron Radiation Center (University of Wisconsin), consisting in a dedicated pulsed laser deposition system, which enables us to grow thin films with excellent surface quality. Our sample transfer procedures assure that this surface quality is not affected on the way to the ARPES analyzer, which is connected to a beamline.

We have built a similar film growth system at the EPFL with the aim to connect it to the SCIENTA analyzer at the IPN and to an analyzer on a beamline at the SLS in Villigen.

For the first time we were able to perform ARPES measurements on in-situ grown films of HTSC. Previously to our work all the ARPES measurements were carried out on cleaved or scraped samples, predominantly single crystals of $Bi_2Sr_2CaCu_2O_8$ compounds. Thin films offer the possibility to study the effect of epitaxial strain induced through lattice mismatch between the film and its substrate. Compressive strain in the CuO_2 plane has been known to enhance the critical temperature (T_C) up to 50%, therefore we expected to see a signature of strain in the electronic dispersion.

The Fermi surface of unstrained $La_{2-x}Sr_xCuO_4$ evolves with doping as reported for scraped single crystals, but also changes strongly with strain. Our studies show, that the in-plane compressive strain changes the Fermi surface topology from hole-like to electron-like. It enhances band dispersion and the Fermi level is crossed before the Brillouin zone boundary, in sharp contrast to the "usual" saddle point remaining ~30 meV below the Fermi level measured along the direction of the *Cu-O* bonds on unstrained samples. The associated reduction of the density of states near the Fermi level does not diminish the superconductivity; T_C is enhanced in all our compressively strained samples. This result is rather surprising since such a reduction of the density of states, according to many mean field models, does not favor the increase of T_C measured in our films. By comparing the ARPES measurements on our films with measurements on bulk crystals, we could also show that the results from our relaxed

films are equivalent to those on bulk crystals, therefore excluding an explanation through finite size effects other than strain.

Our latest results on films under huge tensile strain (1% change in c-axis) are significantly different: ARPES shows evidence for a 3-dimensional dispersion, in contrast with the strictly 2-dimensional dispersion observed on compressively strained films.

Already the conduction band of relaxed $La_{2-x}Sr_xCuO_4$ is atypical: It has considerable apical-oxygen p_z and $Cu3d_{z^2-r^2}$ out-of-plane character, while for the rest of the cuprate HTSC, those orbitals hybridize far less with the conduction band. We relate the observed *z*-axis dispersion with the significant displacement of the apical-oxygen towards the CuO_2 plane, induced by the epitaxial strain.

Resistivity measurements show an insulating behavior of films under extreme tensile strain and no T_C. Films with weaker tensile strain still exhibit superconductivity, but diminished as compared to the relaxed films. In summary, while the in-plane compressive strain tends to push the apical oxygen far away from the CuO_2 plane, enhances the 2-dimensional character of the dispersion and increases T_C, the tensile strain seems to act exactly in the opposite direction and the resulting dispersion is 3-dimensional. We have established the shape of the Fermi surface for both cases, yet further experiments are required to clarify fine details.

Résumé

Le sujet de cette thèse est la croissance et l'analyse de couches minces supraconductrices à haute température critique (HTSC), ainsi que l'étude de leurs propriétés électroniques. On s'intéresse tout particulièrement à l'effet des contraintes épitaxiales sur la structure électronique, étudiée essentiellement par spectroscopie de photoémission en résolution angulaire (ARPES). La caractérisation de la structure cristalline de ces films et faite par diffraction de rayons X. Leurs propriétés de transport et leur réponse magnétique sont examinées respectivement à l'aide de mesures de résistivité et de susceptibilité magnétique.

Pour atteindre ces objectifs nous avons développé un système compact, unique en son genre, spécialement dédié à la fabrication de couches minces de haute qualité de surface, pouvant être transférées in-situ vers l'analyseur couplé à une ligne synchrotron. Cette installation a été réalisée au Synchrotron Radiation Center (SRC) de l'université du Wisconsin et vient d'être répliquée avec succès dans nos laboratoires à l'EPFL dans le but de la coupler à l'analyseur SCIENTA de l'IPN. Vu sa compacité elle pourra aussi être transportée facilement au SLS à Villigen.

Nous sommes les premiers à avoir pu faire des mesures ARPES sur des couches minces HTSC fabriquées in-situ. Auparavant la plupart des mesures avaient été réalisées sur des monocristaux $Bi_2Sr_2CaCu_2O_8$ clivés. Les couches minces offrent la possibilité d'induire des contraintes épitaxiales grâce à l'écart des constantes réticulaires entre la couche déposée et le substrat. Il a été montré que les contraintes de type compressif dans le plan CuO_2 ont pour effet d'augmenter la température critique (T_C) de 50% ; on s'attend donc à voir la signature de ces contraintes dans la dispersion électronique.

Comme cela a été démontré sur des monocristaux de $La_{2-x}Sr_xCuO_4$ (surface grattée), la surface de Fermi change avec le dopage (nombre de porteurs par atome de cuivre). Mais, comme le montrent nos travaux, elle change aussi beaucoup avec les contraintes. En effet, sous compression dans le plan sa topologie passe de "type trou" à "type électron".

Les contraintes compressives amplifient la dispersion et la bande franchie le niveau de Fermi à l'intérieur de la limite de la zone de Brillouin, quelque soit la direction dans le plan CuO_2. Ceci est en net contraste avec le comportement dans les échantillons relaxés, où la bande de conduction présente un point selle dans la direction des liaison *Cu-O* et reste ~30 meV en dessous du niveau de Fermi. La réduction de la densité d'états au

niveau de Fermi qui en résulte, devrait d'après des modèles de type champ moyen, diminuer fortement le T_C. Ceci est contraire à toutes les mesures réalisées à ce jour sur ces échantillons où le T_C montre une augmentation nette. En outre, la comparaison des mesures ARPES sur nos couches minces relaxées avec celles effectuées sur des monocristaux massifs nous permet d'exclure une éventuelle explication de ces résultats inattendus invoquant des effets de taille finie autres que les contraintes.

Tout récemment, nos études sur des couches minces sous forte contrainte extensive montrent des effets surprenants, très éloignés de ce que l'on aurait pu attendre sur la base des résultats antérieurs : La photoémission met en évidence une dispersion 3-dimensionnelle, contrairement à la dispersion strictement 2-dimensionnelle observée sur des échantillons sous compression. Cependant ces résultats semblent bien s'accorder avec certaines particularités connues de la bande de conduction du $La_{2-x}Sr_xCuO_4$. Parmi tous les cuprates HTSC, le $La_{2-x}Sr_xCuO_4$ est celui dont l'oxygène apical est le plus proche du plan de CuO_2, favorisant l'hybridation de l'orbitale p_z de cet oxygène apical avec l'orbitale $Cu3d_{z^2-r^2}$ (hors du plan). Le rapprochement de l'oxygène apical du plan de CuO_2 sous la contrainte augmenterait le recouvrement de ces orbitales ouvrant ainsi un canal de conduction dans la troisième dimension.

Des mesures de résistivité montrent un comportement isolant pour des couches minces sous contrainte extensive extrême et pas de T_C. Des couches minces sous contrainte extensive plus faible montrent de la supraconductivité, mais diminuée par rapport aux couches relaxées. En résumé, la compression tend à pousser l'oxygène apical loin du plan de CuO_2, il renforce le caractère 2-dimensionnel de la dispersion et augmente T_C. La contrainte extensive semble agir dans le sens opposé et la dispersion résultante est 3-dimensionnelle.

Chapter 1: Introduction

The purpose of this thesis is to examine the electronic structure of high temperature superconductors (HTSC) by angle resolved photoemission spectroscopy (ARPES) measurements. Particularly the huge effect, that strain has on the critical temperature, captured our interest, and so we dedicated our efforts to the investigation of the electronic structure of HTSC under strain. For this purpose we built an experimental chain starting with the production of our HTSC films in a pulsed laser deposition (PLD) system. From there they can be transferred in-situ to an analyzer chamber for ARPES measurements, performed with synchrotron light. The advantage of this procedure is that we can optimize the quality and adjust the properties of the films to our needs. Therefore, we are able to carry out ARPES measurements on HTSC under strain, a property that is inherent to thin films and cannot be measured in bulk crystals. Moreover, we do not have to cleave the samples, but can measure them as-grown.

In what follows I would like to present the structure of this thesis. In this chapter I will position our work in the field of superconductivity. First this will be done with a historical overview, which at the same time illustrates some of the fundamental questions in superconductivity and how they have been attacked. This historical overview goes over to a sketch of the present situation, divided into two parts: a theoretical and an experimental part.

Even if in the frame of this thesis I am not entering far into theoretical matters, I will present also some theoretical approaches that are commonly used, since our measurements were also employed by theoreticians to check their models [1.1].

Then an overview of the experimental techniques, that are used to elucidate all possible aspects of superconductivity, is given. Some of these techniques are used by other groups for measurements on films grown on our PLD system.

Finally some information on HTSC in general and on $La_{2-x}Sr_xCuO_{4+\delta}$ in particular is given. $La_{2-x}Sr_xCuO_{4+\delta}$ is the material with which most of our measurements have been performed. We chose $La_{2-x}Sr_xCuO_{4+\delta}$ because strain can have a very strong influence on its structure and electronic properties.

PLD is discussed in chapter 2; our PLD system and the film growth procedure are presented in detail. Chapter 3 describes the characterization of the grown films by X-ray diffraction and the search for optimal growth conditions with the objective to produce films suitable for ARPES measurements.

Chapter 4 explains the procedures applied to the measured ARPES data for the extraction of information on the electronic dispersion.

Chapters 5 and 6 finally present ARPES measurements on $La_{2-x}Sr_xCuO_{4+\delta}$ films under compressive and tensile strain, respectively, and for different doping levels. Both deliver surprising results concerning the evolution of the electronic structure. The Fermi surface changes from hole-like for relaxed films and bulk crystals to electron-like for films under compressive strain. For films under tensile strain, the Fermi surface acquires a 3-dimensional character. T_C increases under compressive strain and decreases under tensile strain. For very strong tensile strain T_C can even vanish.

1.1 Brief History of Superconductivity

For nearly a century the phenomenon of superconductivity is known by physicists and it is still a very active research domain. There is no satisfying explanation for the origin of superconductivity in all superconducting materials, especially HTSC leave many questions open.

At the beginning of superconductivity are the resistivity measurements on mercury performed by H. Kamerlingh Onnes at the Leiden university in 1911 [1.2]. Just a couple of years before, he had succeeded to liquefy helium and was therefore able to reach very low temperatures. Since at that time no proper theory of metals existed, the electronic behavior at lowest temperatures should be verified with these measurements. Instead of the different behaviors that were discussed [1.3], H. Kamerlingh Onnes found a complete vanishing of the resistivity at 4.2 K. Soon other metals were discovered to exhibit superconductivity and it was observed that a sufficiently strong magnetic field or current can destroy superconductivity.

Besides the zero-resistivity, there is a second distinguishing characteristic of a superconductor: perfect diamagnetism. This discovery was made by Meissner and Ochsenfeld in 1933: they observed that a weak magnetic field was expelled from a superconductor when it was cooled below the critical temperature. This was called the Meissner-Ochsenfeld effect [1.4].

The origin of superconductivity remained a mystery for decades and theoreticians needed some time to find models that could describe successfully the observed features. The Meissner-Ochsenfeld effect inspired F. and H. London to develop a model [1.5]. Their model describes the penetration of an external magnetic field in a superconductor.
A very successful phenomenological theory is the Ginzburg-Landau theory [1.6], it is able to describe the characteristic properties of many superconductors, also HTSCs. However, the microscopic origin of superconductivity was still unexplained.
In the meantime several new materials were found that exhibit superconductivity – pure elements as well as compounds – and the maximal critical temperature, at which zero resistivity appeared, increased slowly.

A major theoretical breakthrough was achieved in 1957 with the BCS theory presented by J. Bardeen, L. Cooper and R. Schrieffer [1.7]. It is a microscopic theory that takes into account an attraction between electrons. When the superconductor is cooled below T_C, the BCS theory predicts the condensation of correlated pairs of conduction electrons carrying the supercurrent. These electron pairs are called Cooper pairs and their binding energy is at the origin of the energy gap, which appears at the Fermi level in the superconductive state. The Cooper pairs are described by a single wave function and move coherently. They are not scattered by impurities and therefore the resistivity in a superconductor is zero.
For some time the BCS theory could explain quite well the properties of most known superconducting materials. It seemed now questionable if superconductivity could be found in materials at room temperature, since BCS would set a limit at much lower temperatures.

Also in the field of applications for superconductivity some advances where made: B. Josephson predicted tunneling effects [1.8], called Josephson effects. Soon his forecasts were confirmed and led to the development of the Josephson junction, widely used in technology based on superconductivity or in SQUIDS, very sensitive magnetic flux detectors. Niobium compounds are used for powerful commercial magnets.

In 1986 K. A. Müller and G. Bednorz started a revolution in superconductivity by discovering a new class of superconductors, the cuprates [1.9]. Some other oxides were already known before, but they have mostly a rather low T_C. The cuprates can show a T_C much higher than the T_C in all materials known at that time. In the following years, the T_C rose fast and culminated in Hg compounds ($HgBa_2Ca_2Cu_3O_{8+\delta}$ has a T_C of 133 K [1.10], under a pressure of 30 GPa it reaches even 164 K [1.11]). A next surprise followed in 2001 with the discovery of superconductivity in MgB_2 with a T_C close to 40 K, but easier to handle than cuprates [1.12].

1.2 Theoretical Background

For the description of the material that we are studying, $La_{2-x}Sr_xCuO_{4+\delta}$, the BCS theory is unfortunately not adequate. There are several properties of cuprates that the BCS theory cannot explain, like their pseudogap or their non-Fermi liquid properties.
The theoreticians replied by developing a large number of models and theories to explain the behavior of the cuprates, but until now there is no theory that reproduces all observed features [1.13].

Theoreticians are still arguing over the question, which interaction mechanisms are responsible for superconductivity in HTSC. The standard electron-phonon picture from the BCS theory does not seem suitable anymore for the role of the essential mechanism leading to HTSC. To replace the phonon, several propositions have been made, but none was unanimously accepted. Among a variety of suggestions, there were phonons with anharmonic behavior, bipolarons [1.14], charge fluctuations or spin fluctuations [1.13].

In the following some theoretical approaches are presented, which have been used for $La_{2-x}Sr_xCuO_{4+\delta}$ and other HTSC. Since we do ARPES measurements, we are especially interested in band structure calculations, to which our measurements are compared.

Many models for superconductors are based on the tight-binding approximation. It is an intermediate case between the nearly free electron approximation with a weak potential, which is leading to broad and overlapping energy bands, and the situation where the potential is dominant and therefore the orbitals are centered on individual atoms. In the tight binding approximation the valence electron orbitals of neighboring atoms overlap.

The overlap is small enough to preserve the identity of the individual atomic contribution and narrow bands are formed.

For the interpretation of our ARPES data, we developed an approach where the energy is written as a Fourier series. The resulting expression can be compared to the expression from the tight binding approach. Therefore we refer to our approach also as "generic tight binding approach".

Many models are frequently used to describe HTSC, for example the Hubbard model and its descendants [1.15], which take into account electronic correlations.

Sophisticated models, adapted to specific interesting materials have been developed. To check the validity and accuracy of these models, they are often compared to experimental measurements, particularly to photoemission. The data from our ARPES measurements on $La_{2-x}Sr_xCuO_{4+\delta}$ films under compressive strain have for instance been fitted with the Emery model (see [1.1], [1.16]).

The results from band calculations based on such models offer insight to many properties of superconductors. Nevertheless, there are limitations, and the results are more phenomenologically descriptive than quantitatively predictive.

There exist also other approaches for the description of superconductors, like the topological approach in [1.17] or an approach based on 2-dimensional overscreening of the Coulomb potential [1.18].

1.3 Experimental Techniques

Not only the number of theories and models increases continuously, but also the number of measurement techniques used to investigate superconducting materials. Some of these measurement techniques are listed here (an overview is given in [1.19]).

The interest in transport measurements resides in the importance of the transport properties of a superconductor for applications. There are among others resistivity and magnetoresistivity (T_C, critical current, critical field), susceptibility, Hall effect (carrier concentration, mobility), tunneling (gap) and thermal conductivity measurements.

Spectroscopic measurement techniques include Raman and Infrared spectra (vibrational transitions, gap), photoemission spectroscopy, among which ARPES (electronic structure), X-ray absorption spectroscopy, such as EXAFS (extended X-ray absorption fine-structure, used to determine distance and coordination of atoms surrounding the atom whose absorption edge is examined) and XANES (X-ray absorption near-edge structure, unoccupied orbitals and site symmetry), inelastic neutron scattering (phonon dispersion curves and density of states).

Another family of spectroscopic measurement techniques is magnetic resonance, to which belong among others nuclear magnetic resonance (local environment of the nucleus), microwave absorption (gap), muon-spin relaxation (phonons, penetration depth) and Moessbauer Resonance (local chemical and magnetic environment).

Some of these measurements are being performed by other groups on our samples, for example EXAFS, Raman spectroscopy, microwave and reflectivity measurements.

Each of these techniques is used to elucidate one facet of superconductivity. The aim of this venture is to increase the comprehension of the phenomenon by assembling the contributions from all the different fields.

1.4 Our Approach

In this section I would like to situate our activities in the field of superconductivity research and among all the approaches described in the previous paragraphs.

For our investigations we chose among the experimental techniques ARPES. It is particularly interesting because it is the most direct method to determine the electronic band structure. We focus on the influence of strain in HTSC, especially how it affects the electronic dispersion near the Fermi level.

ARPES is done with light in the ultraviolet or X-ray range. One can work with helium-gas discharge tubes where only fixed energies (21.2 eV and 40.8 eV) are available. More suitable it is to work with the light from a synchrotron, that can be tuned in energy and that is orders of magnitude more brilliant [1.20]. We performed our measurements at the Synchrotron Radiation Center in Stoughton.

ARPES has very high requirements for sample quality, especially for its surface. Therefore we had to develop and optimize a film growth system. We constructed a Pulsed Laser Deposition (PLD) system on which we are growing films of HTSC materials. Once the film is grown, it is transferred in-situ to the analyzer chamber where the photoemission measurements are done.

Most ARPES measurements on HTSC have been done with $Bi_2Sr_2CaCu_2O_8$, because it is easily cleavable and thus very well adapted for ARPES [1.21]. Other HTSC materials can only be cleaved or scraped and are much more difficult to measure. Our in-situ transfer allows us to extend ARPES measurements to non-cleavable materials, that before where known to be not very suitable for ARPES, as for example $La_{2-x}Sr_xCuO_{4+\delta}$.

Another advantage of a PLD system is its small size and its mobility, since there is only very limited place available in the vault of the synchrotron (SRC).

Other film growth techniques like molecular beam epitaxy (MBE) and ion beam sputtering are more space requiring and less versatile.

Once the huge experimental obstacles are overcome, the combination of film growth, in-situ sample transfer and ARPES measurements opens new horizons for the exploration of HTSC and related oxides. Therefore other groups followed us soon by performing ARPES measurements on films grown by PLD or MBE [1.22, 1.23].

1.5 High Temperature Superconductors

HTSC like $La_{2-x}Sr_xCuO_{4+\delta}$ have a perovskite type structure and many of them are cuprates [1.24]. The common feature of the cuprates is their anisotropy and their layered structure with the CuO_2 planes (see figure 1.1). The CuO_2 plane gives them also their name. Their role is crucial for the electronic properties, which we are investigating.

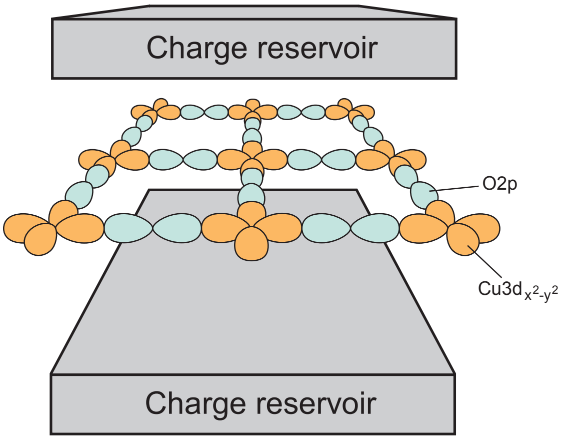

Figure 1.1: CuO_2 plane in HTSC

Above and below the CuO_2 planes, there are layers, consisting in a cation (La^{3+} in $La_{2-x}Sr_xCuO_{4+\delta}$) that forms an ionic bond with oxygen to which it transfers its valence electrons. These layers are called charge reservoir layers and are responsible for the doping with holes or electrons. In contrast with most other oxides the cuprate HTSC show metallic behavior at room temperature. The conductivity is metallic in the CuO_2 planes, perpendicular to these planes it is much smaller.

The CuO_2 planes have a covalent character and are responsible for the conduction. The *3d* electrons are the valence electrons in copper. Their electronic charge distribution is illustrated in figure 1.2, each orbital can be occupied by two electrons of opposite spin.

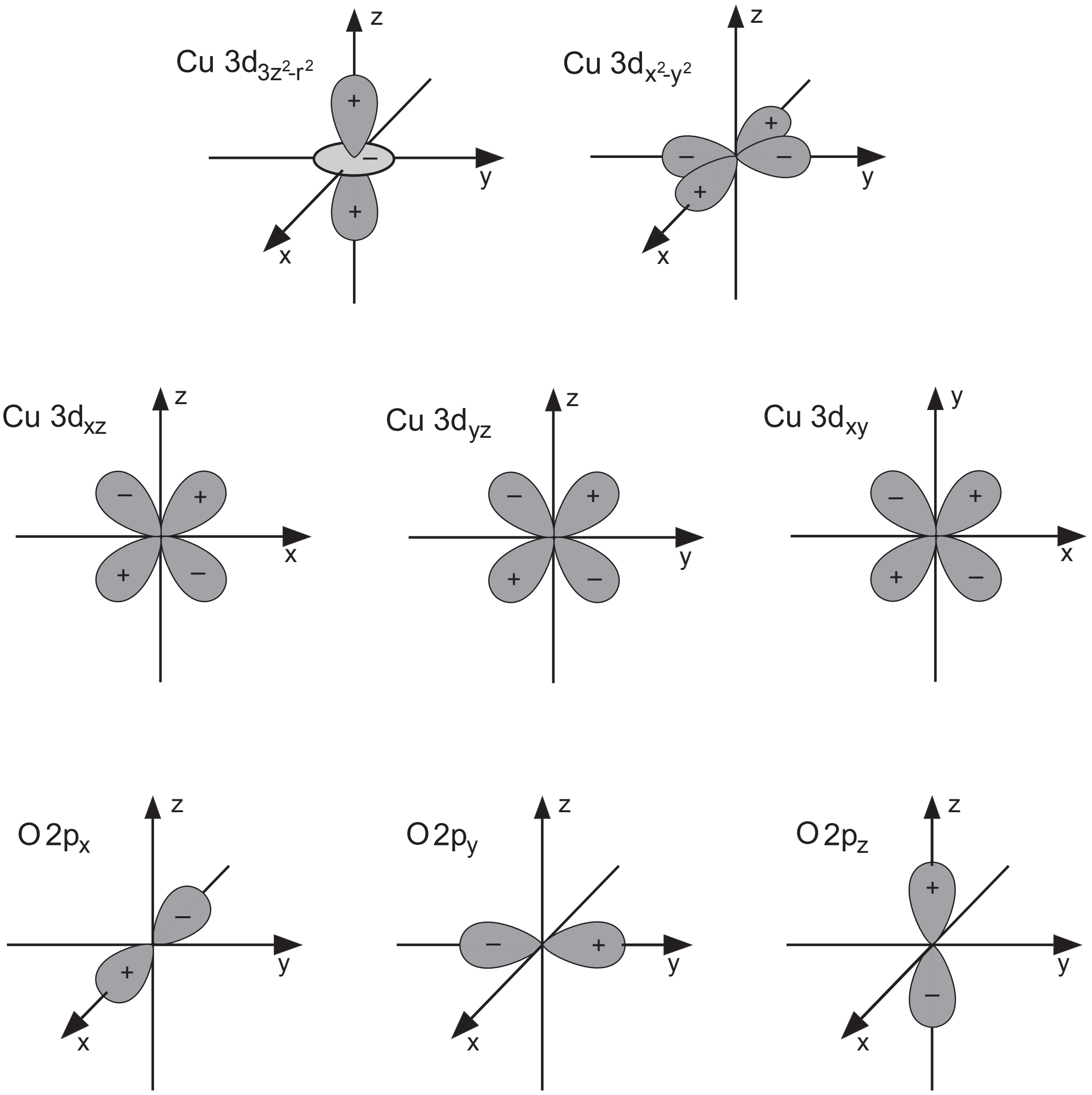

Figure 1.2: The Cu3d and O2p orbitals

The oxygen valence electrons are the *2p* electrons. The strong Coulomb interaction between the *Cu3d* electrons and the close energy levels of the *Cu3d* and the *O2p* electrons lead to a covalent character of the *Cu-O* bond. The crystal field splits the *Cu3d* orbitals into an e_g and a t_{2g} level, which are further split into 4 sublevels. The *O2p* orbitals undergo a splitting into a σ and two π levels.

The bonds in the CuO_2 planes are formed by hybridization of the copper $3d_{x2\text{-}y2}$ orbitals and the oxygen σp orbitals, as illustrated in figure 1.3.

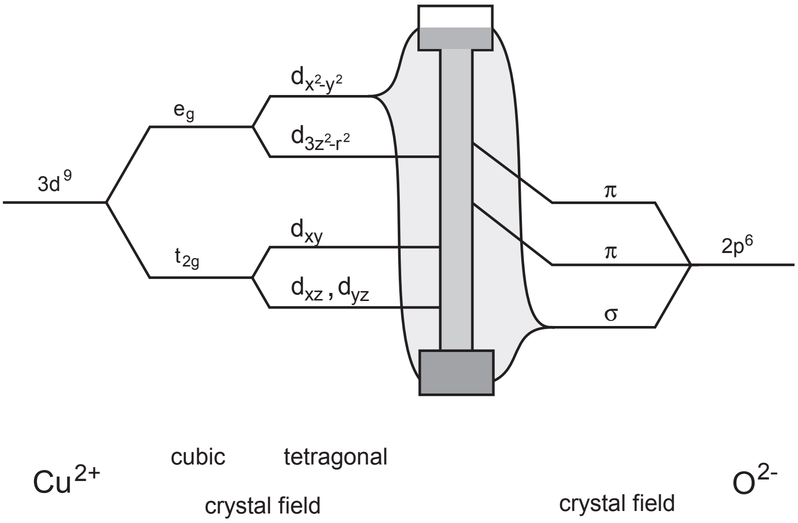

Figure 1.3: Crystal field splitting of the copper and oxygen orbitals and hybridization of the copper $3d_{x2\text{-}y2}$ *orbitals and the oxygen* σp *orbitals*

For the stoichiometric parent compounds of the cuprates (for example La_2CuO_4 in the case of $La_{2-x}Sr_xCuO_{4+\delta}$) an insulating, antiferromagnetic behavior is observed experimentally. This is a consequence of the strong correlations due to the Coulomb interaction on the *Cu3d* sites [1.25].

By doping with electrons or holes, the material will undergo a transition from the antiferromagnetic insulator to a pseudogap phase and then to a normal metal, or at low temperatures to a superconductor (see figure 1.4). In the pseudogap phase superconductivity is not present, but anomalous effects appear, like a partial suppression of the density of states at the Fermi level. Doping can occur either through substitution of

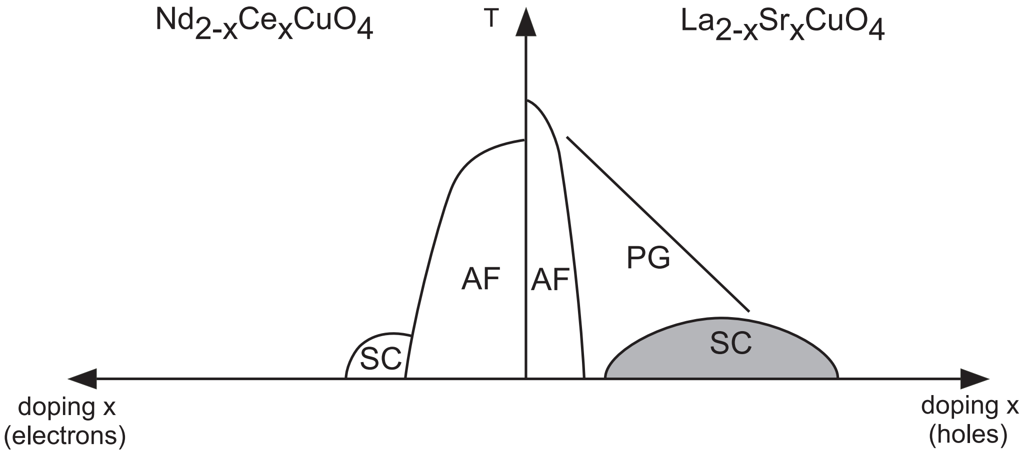

Figure 1.4: Phase diagram of $La_{2-x}Sr_xCuO_4$ *(and its electron-doped counterpart* $Nd_{2-x}Ce_xCuO_4$*). SC is the superconducting phase, AF the insulating antiferromagnetic phase and PG is the pseudogap phase.*

an atom by an atom with different valence (La^{3+} substituted by Sr^{2+} in $La_{2-x}Sr_xCuO_{4+\delta}$) or by a modification of the oxygen content ($La_{2-x}Sr_xCuO_{4+\delta}$).

In the superconducting phase, the doping level at the highest T_C is called the optimal doping. A superconductor with a lower or higher doping level is called underdoped or overdoped respectively. Not only doping, but also strain affects strongly the T_C, as we will see in chapter 5 and 6.

1.6 $La_{2-x}Sr_xCuO_{4+\delta}$

The material on which we focused our attention is $La_{2-x}Sr_xCuO_{4+\delta}$. It exhibits several features that make it the ideal superconducting material for our research. For example it can be doped over a wide range by *Sr* substitution on *La* sites (from $x = 0$ to about $x = 0.3$). Also the influence of strain is more pronounced than in other materials. Moreover $La_{2-x}Sr_xCuO_{4+\delta}$ films are suitable for ARPES measurements in contrast to $YBa_2Cu_3O_{7-\delta}$ films for example, which present enormous obstacles to ARPES [1.26].

Among the HTSC cuprates $La_{2-x}Sr_xCuO_{4+\delta}$ has one of the simplest unit cells. $Bi_2Sr_2Ca_2Cu_3O_{10+\delta}$ and similar compounds have many layers more. $Bi_2Sr_2CaCu_2O_{8+\delta}$, popular for ARPES studies, has a superlattice modulation along its *b*-axis, which leads to a complicated electronic band structure, with the appearance of shadow bands in ARPES spectra [1.27].

Another property of $La_{2-x}Sr_xCuO_{4+\delta}$ that will reveal important for us is the fact that the distance between the copper atom and its apical oxygen is smaller than in all the other HTSC cuprates.

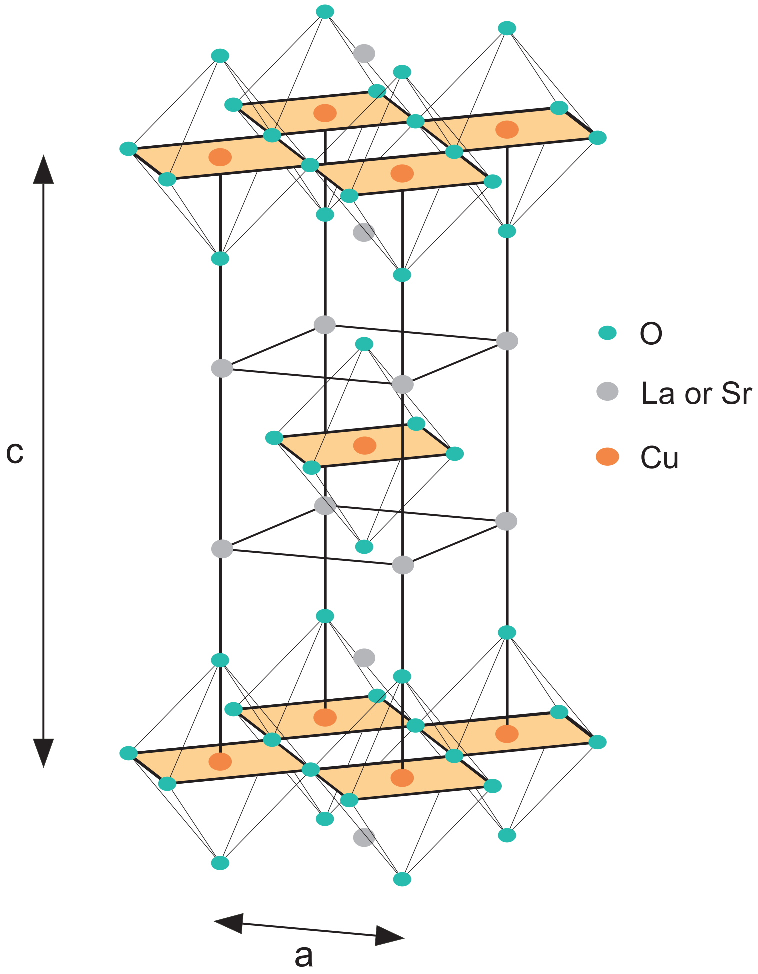

Figure 1.5: $La_{2-x}Sr_xCuO_4$ *unit cell with symmetry I4/mmm. In the corner of each octahedron, surrounding the Cu atom, an O atom is located. The O atoms in the upper and the lower corner are the "apical oxygens".*

The structural properties of $La_{2-x}Sr_xCuO_{4+\delta}$ have been studied in detail by Radaelli et al. [1.28]. The structure of the unit cell of $La_{2-x}Sr_xCuO_{4+\delta}$ is shown in figure 1.5. The unit cell has the body centering symmetry, it consists in two identical blocs, one above the other and shifted by half a lattice constant in the *x* and the *y* direction. Besides the 4 oxygen nearest neighbors in the CuO_2 plane, the *Cu* atom has also two apical oxygen atoms as nearest neighbors. The *La* atoms are located in a plane close to the one of the apical oxygen. According to the doping level, *Sr* atoms replace some of the *La* atoms. The *Sr* doping level *x* is usually well known. On the other hand, the oxygen deficency or excess δ is much less controlled by crystal growth procedures and it is difficult to be determined. For bulk crystals a thermogravimetric analysis has been performed in [1.28]. For doping levels between $x = 0.1$ and $x = 0.2$, they measure a small oxygen deficiency: $-0.02 < \delta < 0$. We assume that δ is small in our films, hence it is omitted in the chemical formula, from now on it will be written $La_{2-x}Sr_xCuO_4$. Nevertheless, it must be verified if a small δ is in agreement with the data from the ARPES measurements on our films.

Strain can be induced through hydrostatic pressure or through lattice mismatch between a substrate and the HTSC thin film, which is grown on the substrate. Since we grow thin films by PLD, we make use of the possibility to explore the effects of epitaxial strain. A compression in the plane of growth (in our $La_{2-x}Sr_xCuO_4$ films this plane is parallel to the CuO_2 planes and contains the *a*- and *b*-axis) leads to an expansion of the *c*-axis as it is illustrated in figure 1.6. The contrary happens when tension is applied in the plane: then the *c*-axis decreases. In-plane compressive strain can enhance the T_C, whereas tensile strain diminishes it.

The effect of strain in high T_C cuprates was initially demonstrated by Naito et al. [1.29] and Locquet et al. [1.30] who have shown that in $La_{2-x}Sr_xCuO_4$ films the T_C can be enhanced by 50%.

Bozovic et al. [1.31] have shown that it is important to saturate the films with oxygen ($\delta > 0$). This oxygenation combined with the growth induced strain, enhances T_C in $La_{2-x}Sr_xCuO_{4+\delta}$ films up to 51K [1.31]. We were able to confirm the T_C enhancement by compressive strain in thin $La_{2-x}Sr_xCuO_4$ films and also the decrease or even suppression of T_C in films under tensile strain.

The mismatch of the atomic distances in the CuO_2 plane and in the LaO (SrO) plane leads to buckling in both planes and to orthorhombic distortions. The orthorhombic phase

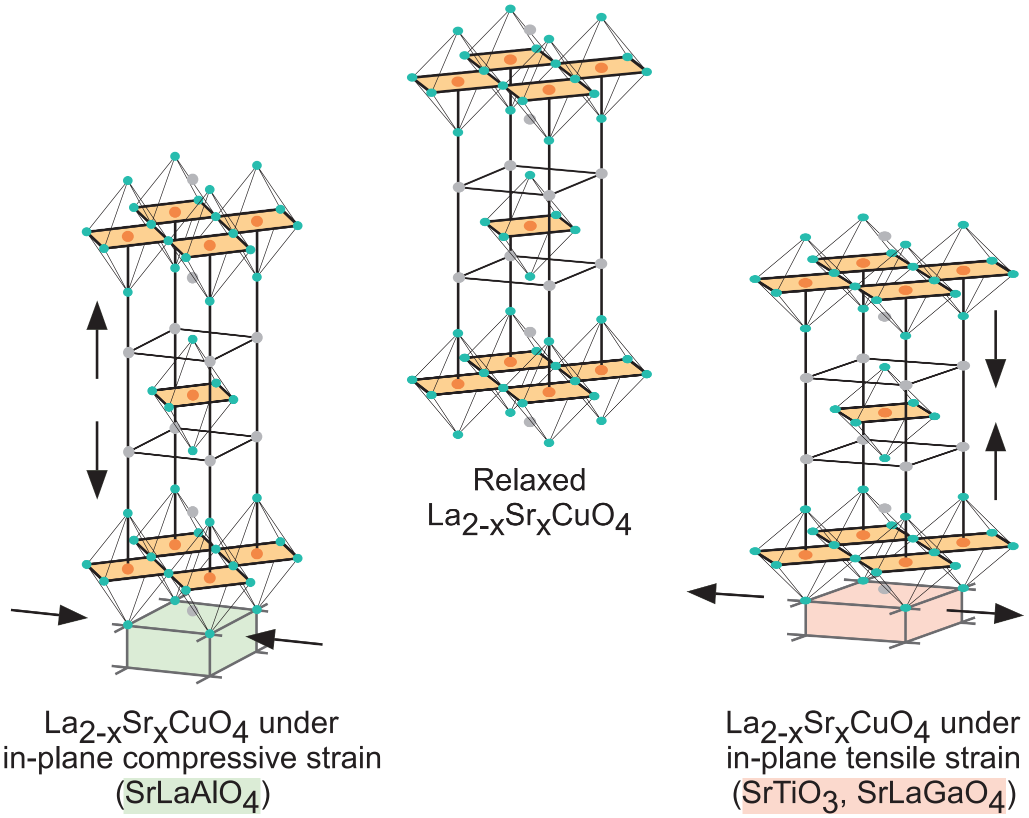

Figure 1.6: Lattice mismatch between substrate and film induces compressive in-plane strain together with an extension along the c-axis (left), or tensile in-plane strain with a compressed c-axis (right).

appears at low temperatures and for low doping, it can lead to a difference between the *a*-axis and the *b*-axis of up to 2%. However, for films with x = 0.15 (optimally doped) and x = 0.20 (overdoped), like the films discussed in chapters 5 and 6, the difference between the *a*-axis and the *b*-axis does not exceed 0.5%, even at the low temperatures of our ARPES measurements (11 K) [1.28]. Therefore we assume that our films are tetragonal.

Imperfections like impurities are always present, even in the best single crystals and their influence on the physical properties should not be neglected.

The ARPES data measured on our $La_{2-x}Sr_xCuO_4$ films are compared to data on bulk samples. Thus it must be emphasized that HTSC films differ usually from bulk single crystals even when they are of the highest quality [1.32]. Namely, it is often difficult to fully oxygenate single crystals, and there is always a certain amount of growth induced strain and disorder in the films [1.33].

Chapter 2: Pulsed Laser Deposition

All the films on which we performed ARPES measurements have been grown by the pulsed laser deposition (PLD) technique. In this chapter I will first present PLD in general and than introduce our PLD system at the SRC with its particular features that make it suitable for subsequent in-situ ARPES measurements.

The heart of a PLD system is its laser. Some of the properties of laser light are the narrow bandwidth in frequency, the coherence, the high spatial resolution and the high power density. These characteristics lead to a broad range of applications in materials processing. In industry it is used for welding, heat treatment of surfaces or patterning. It can vaporize the hardest and most heat resistant materials. This property allows using a laser for the deposition of thin films on a substrate, by evaporating the surface of a chosen target. Pulsed laser deposition becomes more and more popular, because it allows depositing materials of complex stoichiometry, which makes it very interesting for the production of HTSC films. Reference [2.1] gives a comprehensive overview of the PLD technique.

The following historical summary traces the steps and technical developments that lead to PLD and illustrates at the same time the main features of this technique.

2.1 Historical Development of PLD

In 1916 Albert Einstein was studying the absorption of light and came to the conclusion that besides absorption and spontaneous emission there should also exist the stimulated emission [2.2]. About 40 years later this idea could finally find its way to a practical application. In 1953 C. Townes constructed the first maser (microwave amplification by stimulated emission of radiation) [2.3] and in 1960 the first laser was built by T. H. Maiman [2.4]. Another five years later Smith and Turner used a ruby laser to deposit thin films, the pulsed laser deposition was born [2.5]. However, the quality of lasers at that time was not good enough for the production of thin films, the stability output was poor and the repetition rate too low. Other techniques like molecular beam epitaxy (MBE) produced films of much better quality. Some years later, with the fast progress in laser technology also PLD became competitive for laboratory use.

Lasers have now a higher repetition rate and Q-switches allow the generation of very short and intensive pulses, the key ingredient to insure the transfer of the same stoichiometry from the target to the film, which can grow epitaxially on a chosen substrate [2.1]. The advances in the development of harmonic generators made it possible to use ultraviolet light for the ablation. In the ultra-violet range the absorption depth is shallower. With the development of the excimer and the Nd-YAG lasers it is now possible to grow thin films of very high quality.

The first superconducting $YBa_2Cu_3O_{7-\delta}$ thin films have been grown by PLD back in 1987 [2.6]. This event marked a breakthrough for PLD and since then, many materials that are normally difficult to deposit by other methods, in particular polycomponent oxides, have been successfully deposited by PLD. Crystalline films can be grown epitaxially on an appropriate substrate. Besides Ceramic oxides, metallic multilayers and various superlattices have been grown [2.7]. More recently, PLD has also been used to produce nanotubes or quantum dots [2.8, 2.9].

2.2 Mechanisms of PLD

The main advantage of PLD comes from the mechanism by which the laser removes the target material. PLD relies on a radiation-matter interaction, resulting in formation of a plasma plume on any target material. Although the physical processes taking place on the target are quite complex, one can consider the following simple picture:

The strong absorption of the laser radiation by the solid surface leads to a fast evaporation of the target materials. These evaporated materials consist of highly exited and ionized particles. They form a glowing plasma plume originating on the target surface. Thermal evaporation leads to a vapor composition depending on the vapor pressures of the elements in the target. On the other hand, in the case of PLD, the laser induced evaporation produces a plume which is similar to the target in its stoichiometry.

This is the result of the extremely high heating rate of the target surface due to the pulsed laser irradiation. Because of the high heating rate of the ablated materials, laser deposition of crystalline film can be done at a relatively low substrate temperature compared to other film growth techniques.

During the production of films, a relatively high partial pressure (300 mTorr) of reactive gas, such as oxygen or ozone can be present. The reactive gas can help bind volatile elements to a substrate, preserving the film stoichiometry. It is very important to maintain the appropriate oxygen content in the film during deposition of many oxides. However, the oxygen concentration in the film is less well known than the concentrations of the other elements. This fact is important for the doping of a film. In our $La_{2-x}Sr_xCuO_{4+\delta}$ films, the Sr content x is normally well known and corresponding to the target stoichiometry. The oxygen deficiency (negative δ) or the additional interstitial oxygen (positive δ), is unknown, although it is supposed to be small. The uncertainty about our oxygen doping will be further discussed in chapter 5.

Indeed, PLD is so straightforward that only a few parameters, such as laser energy density and pulse repetition rate, oxygen pressure, substrate Temperature and its distance to the target need to be controlled during the film growth. The targets used in PLD are small compared to the large size required for other sputtering techniques. It is not very complicated to produce multilayer structures of different materials by alternating ablation of different targets arranged on a target carrousel [2.7]. By controlling the number of pulses, a fine control of film thickness down to an atomic monolayer can be achieved [2.10].

In spite of the mentioned advantages of PLD, there are also some weaknesses going together with this deposition technique. One of the major problems is the deposition of droplets on the films.

The presence of the droplets results from the splashing effect, which brings the melted droplets or detached fragments of the target to the film surface. The size of the droplets may be up to a few micrometers. Such droplets affect the growth of the following layers as well as the properties of the film. Other problems of PLD are the narrow angular distribution of the ablated material, which is generated by the adiabatic expansion of the plasma plume, and the pitting on the target surface. These features limit the usefulness of PLD in producing large area uniform thin films, and PLD is not widely employed in industry. Using off-axis geometry or inserting a shadow mask is an effective measure to prevent large droplets. Rotating both the target and substrate can help to produce large area uniform films.

2.3 Models for PLD

To describe what happens during PLD, one can distinguish 3 different steps [2.1], which are schematically shown in figure 2.1:

- the interaction of the laser radiation with the target
- the transfer of the ablated material to the substrate
- the deposition on the substrate, the nucleation and growth of the film.

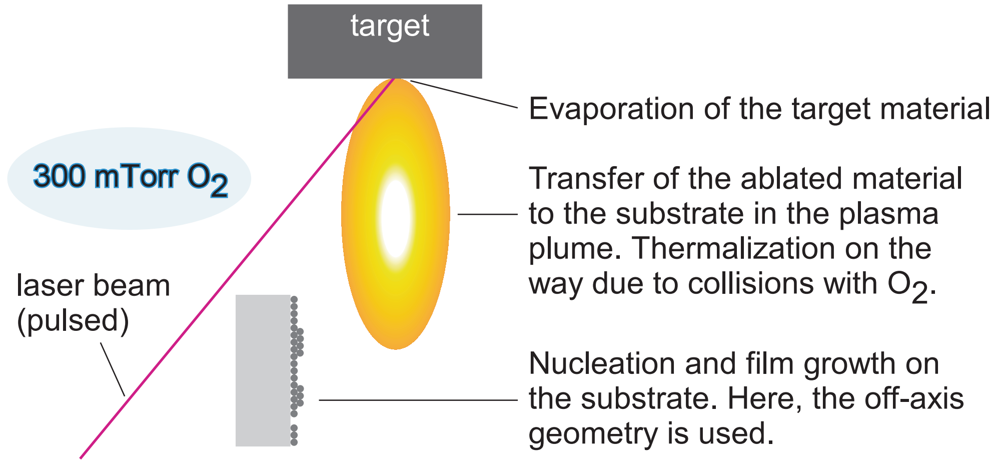

Figure 2.1: The three steps in the PLD film growth process

In the first, step laser pulses of short duration are focused on the target so that high energy densities are achieved. All the constituents in the target are heated to evaporation temperature, so that the stoichiometry is not changed. In the second step, the ablated materials move towards the substrate following the laws of gas dynamics.

The species that impinge on the surface may induce damage: Atoms are sputtered from the surface and form together with the incident material a collision zone. Out of this thermalized region particles nucleate on the surface and film growth occurs.

In the presence of 300 mTorr oxygen, the material reaching the substrate is thermalized due to collisions on its path. In PLD the vapor has a high degree of supersaturation, ionization and mean kinetic energy. It is important to control these parameters to influence the density and the type of defects.

The nucleation and growth of the films depend on the thermodynamics relating the surface and interface energies of the substrate and the film. There are different models to describe the film nucleation and growth, the most conventional model distinguishes three modes.

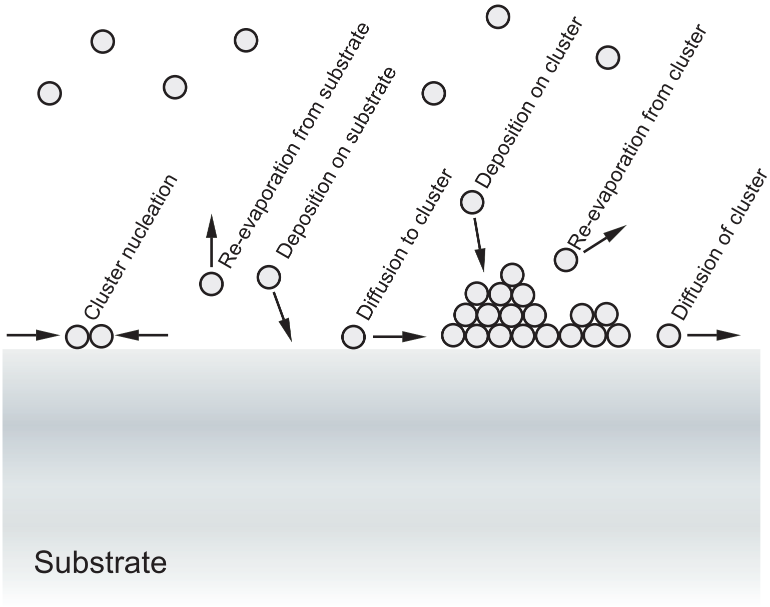

Figure 2.2: Atomic processes participating in the nucleation of clusters on the substrate during film deposition. A change in free energy is associated to each of these processes.

Figure 2.2 shows the different processes that can occur on the substrate surface. Each of these processes is associated with a specific change in free energy.
For a cluster that is large enough, the free energy G can be written:

$$G = a_1 r^2 \Gamma_{c-v} + a_2 r^2 \Gamma_{s-c} - a_2 r^2 \Gamma_{s-v} + a_3 r^3 \Delta G_V \tag{2.1}$$

where the Γ are interface energies, the indices c, v and s stand for the cluster, the vapor and the substrate; r is the cluster radius and a_1, a_2, a_3 are constants depending on the nuclei shape; ΔG_V is the change in volume free energy on condensation of the cluster.

Island Growth

Figure 2.3 illustrates the process of island growth. The surface terms of the free energy in equation (1) are positive, if:

$$a_1\Gamma_{c-v} + a_2\Gamma_{s-c} > a_2\Gamma_{s-v} \tag{2.2}$$

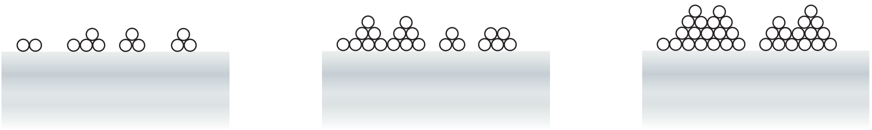

Figure 2.3: Island growth

For three-dimensional cluster growth this is always the case, otherwise it were energetically more favorable for the film to form a single layer on the substrate.

If the surface or interface free energy is decreased or if the volume free energy is increased, then the critical size for a cluster radius decreases. For a smaller radius a cluster can be stable and the cluster nucleation rate will increase.

In practice, this means that a lower substrate temperature does not lower the film formation, but the formation of crystal structure occurs less readily and amorphous phases appear.

Layer-by-layer Growth

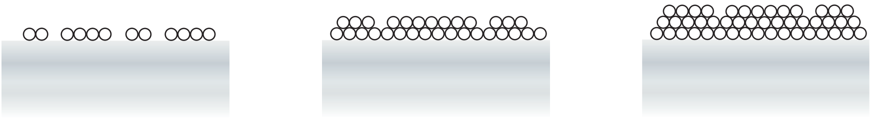

Figure 2.4: Layer-by-layer growth

In the layer-by-layer growth model (see figure 2.4), 2-dimensional islands are formed that are growing in the plane. Before the next layer is formed, complete coalescence is achieved. Homoepitaxy, but also strong film-substrate bonding, low film surface energy and high substrate surface energy can favor monolayer growth. High nucleation density and deposition rate promote also the filling of complete monolayers. The trends for the substrate temperature are the same as in the island growth mode.

Stranski-Krastinov Growth

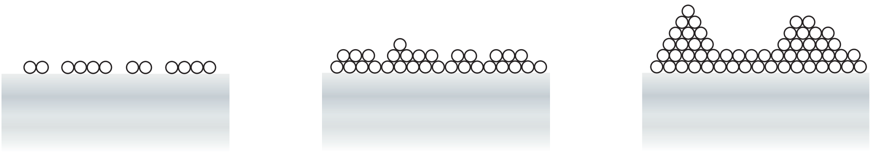

Figure 2.5: Stranski-Krastinov growth

In this model (figure 2.5), after a few layers in the monolayer growth mode, clusters will form and the island growth mode becomes more and more important. For the first layers, the higher substrate surface energy leads to the monolayer growth. Once a few layers deposited, island growth appears because of the lower surface energy of the film.

These models can be applied to the beginning of the film growth or to very thin films. For thicker films more elaborated models exist [2.11, 2.12].
Since substrate surface defects like atomic steps, point defects and dislocations can have a lower energy, they are preferential sites for nucleation and can have a big influence on the growth mode. A good quality of the substrate is therefore crucial.
The parameters that we use to control the film growth modes are essentially the substrate temperature, the partial pressure of oxygen and the target-substrate distance. The aforementioned influences of substrate temperature and deposition rate on the growth mode of the film are illustrated in figure 2.6.

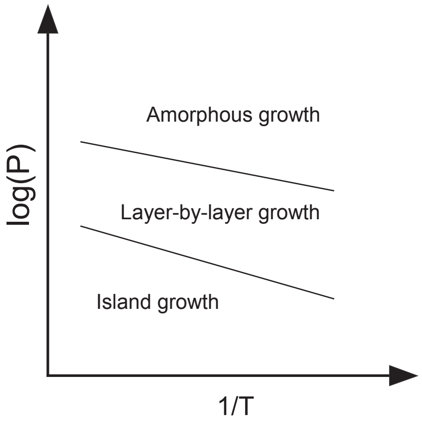

Figure 2.6: The variation of substrate temperature (T) or O_2 pressure (P) can lead to different growth modes

Instead of the deposition rate, the pressure is used, since it is a parameter to which we have access during the film growth. The relation between the deposition rate and the pressure, in our case the partial pressure of O_2, is deduced in [2.13]. When performing PLD we aim at the growth parameters for the layer-by-layer growth mode.

2.4 Our System at the SRC in Madison

Our PLD system was built with the goal to grow thin films for photoemission studies at the Synchrotron Radiation Center (SRC) in Madison. The whole system was designed to be compatible with the photoemission analyzer chamber at the end of the beamline.

Space and mobility requirements were one of the main reasons why we opted for a PLD system rather than for more expensive MBE.

Figure 2.7 shows a picture of our PLD system. The ablation is taking place in the spherical chamber; the sample is mounted on a vertical translator (not visible on the picture, neither is the laser). The laser is situated under the chamber. The laser beam is guided by two wavelength separators and through an ultraviolet-window to the target on the carrousel. The horizontal transfer arm is there to manipulate the sample and transfer it to the suitcase or to the analyzer chamber. The dimensions of the sampleholder are given by the photoemission chamber. The substrate is glued with Epotek H20E (a two-component silver filled epoxy system with good electric and thermal conductivity) on the

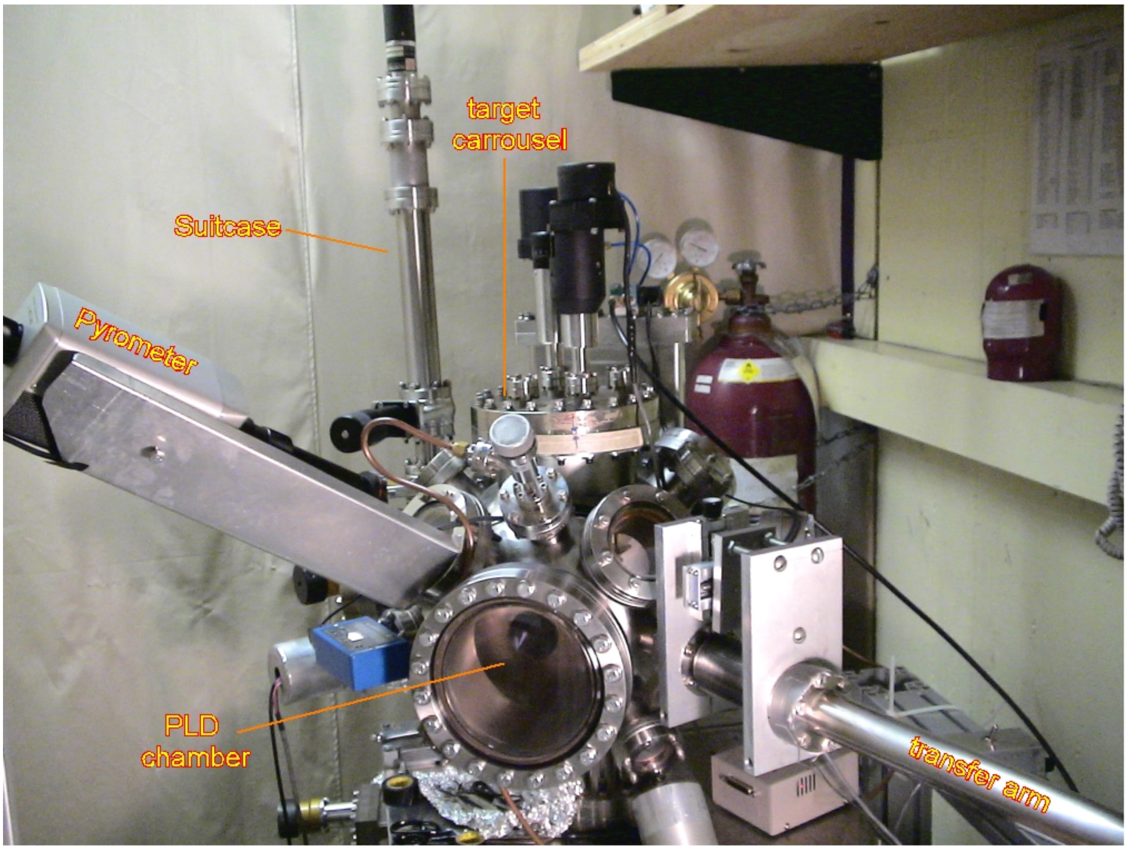

Figure 2.7: The PLD system at the SRC in Madison

sampleholder. The grounding necessary for the photoemission measurements is also assured by Epotek H20E. The substrates that we use are $SrLaAlO_4$, $SrLaGaO_4$ and $SrTiO_3$ from Crystek (see table 2.1). For $La_{2-x}Sr_xCuO_4$ the first one provides compressive strain, whereas the others provide tensile strain.

	a-axis	c-axis	crystallographic structure
$La_{1.85}Sr_{0.15}CuO_4$ (relaxed)	3.778 Å	13.228 Å	tetragonal
$SrLaAlO_4$	3.754 Å	12.636 Å	tetragonal
$SrLaGaO_4$	3.843 Å	12.685 Å	tetragonal
$SrTiO_3$	3.905 Å	3.905 Å	cubic

Table 2.1: Characteristics of the substrates employed for our strained $La_{2-x}Sr_xCuO_4$ films

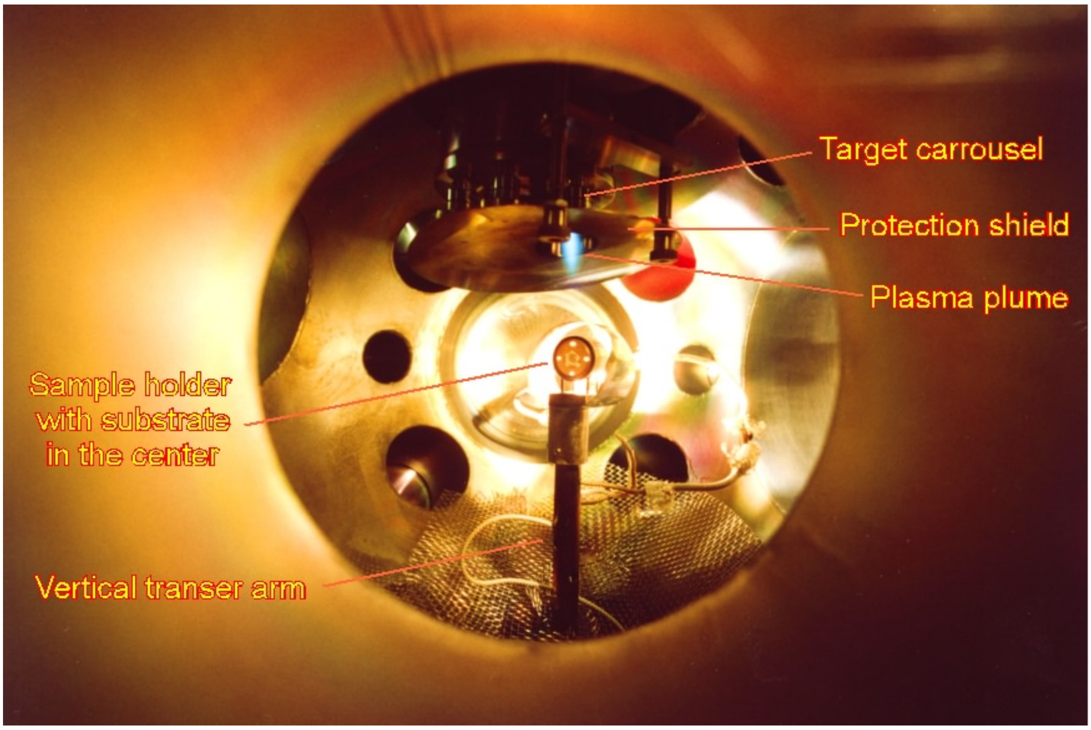

Figure 2.8: Interior of the PLD chamber during the film deposition. The substrate is glued on the sampleholder in the center. The sampleholder itself is mounted on a vertical transfer arm. The light in the chamber is coming from the halogen lamp (inside the sampleholder, not visible), used to heat the substrate. The laser produces the plume on the target. To protect the other targets on the target carrousel, a protection shield is installed.

A picture taken during the deposition process is shown in figure 2.8. To reach the necessary substrate temperature of 600 °C to 800 °C, we use a halogen lamp radiation heater. The temperature is controlled by a calibrated pyrometer. The sampleholder has a hole that is just big enough for a small halogen lamp to fit in and heat it homogeneously. This heater is fixed on a vertical transferarm that can be translated and rotated. A frequency quadrupled Nd-YAG laser (Surelite II from continuum) is used for the ablation. 3.3 pulses per second at a wavelength of 266 nm and an energy per pulse of ~100 mJ give rise to the plasma plume on the target. The target is on a target carrousel with 6 positions. For our $La_{2-x}Sr_xCuO_4$ films we use stoichiometric sintered targets (from HITEC-Materials, the precision of the Sr content is better than 0.01) with doping levels of $x = 0.1$ (underdoped), $x = 0.15$ (optimally doped) and $x = 0.2$ as well as $x = 0.22$ (both overdoped).

We chose the *off-axis* geometry for the deposition. The sample is not perpendicular to the axis of the plasma plume as in common setups, but parallel to it, as it can be seen in figure 2.8. Through this arrangement, we avoid that big droplets are hitting the film surface and we achieve a smoother growth. The deposition rate is decreased compared to the on-axis geometry. It is of the order of a few Angstroms per minute and results in better epitaxy. Target-substrate distances between 4 and 5 cm are used for the growth of our films.

The oxygen pressure during the deposition of the film is 300 mTorr, afterwards it is increased to 1 atm for annealing.

The PLD chamber can be directly linked to the analyzer chamber to do the transfer of the sample under ultra high vacuum conditions. Another solution that we used most frequently was the transfer of the sample in a suitcase filled with high-purity oxygen or under vacuum.

I used this system not only for the growth of $La_{2-x}Sr_xCuO_4$ films, but also for various other materials, such as $Bi_2Sr_{2-x}La_xCuO_6$, manganates ($La_{0.67}Ca_{0.33}MnO_3$) and ruthenocuprates ($RuEu_{1.5}Ce_{0.5}Sr_2Cu_2O_{10}$).

Chapter 3: Film Growth Optimization and Characterization

Our films are produced by PLD and optimized specifically for photoemission measurements without cleavage. Photoemission is a surface sensitive technique and requires very high surface quality. Therefore the films are optimized to get the best surface quality rather than to diminish resistivity or maximize T_C [3.1]. For each material the best growth parameters must be determined. We proceed in the following way for each beamtime dedicated to photoemission measurements: During the weeks preceding a beamtime we produce a series of calibration films, where the growth parameters are systematically monitored and altered. The growth parameters to which we attach most attention are the laser power, the target to substrate distance, the partial pressure of oxygen and the substrate temperature. The samples are then carefully examined by X-ray diffraction, susceptibility and resistivity. The experience acquired with angle integrated photoemission spectroscopy measurements is also helpful [3.2].

In this chapter, the search for optimal growth conditions is illustrated with X-ray diffraction measurements.

The parameters which provide the best films are then taken for the growth of the films used in ARPES.

Only the photoemission measurements can settle if good conditions have been found. For $YBa_2Cu_3O_{7-\delta}$ films under strain, our group had optimized the growth parameters and achieved surfaces of very high quality, as confirmed by X-ray diffraction, resistivity and scanning electron microscopy, but because of oxygen loss in the chains at the surface, ARPES measurements were not successful [3.3, 3.4]. This was also a reason to turn towards $La_{2-x}Sr_xCuO_{4+\delta}$, on which ARPES measurements could eventually be performed.

During the photoemission measurements, properties like strain and thickness of the film are not exactly known. Since photoemission is done in-situ, directly after the deposition of the film, measurements for characterization can only be performed later. For a couple of selected films, X-ray diffraction can be done during the beamtime, but most films were studied afterwards, at the EPFL.

3.1 X-Ray Diffraction

X-ray diffraction is the most important tool to characterize our films [3.5, 3.6]. We use θ-2θ scans to determine the strain and to verify if unwanted phases or non-epitaxial regions are present in the film. If the film quality is good, i.e. if the surface presents no (or a low) roughness, finite size oscillations appear in the spectra and the thickness of the film can be determined by fitting the lobes. The layer-by-layer growth mode leads to finite size oscillations, whereas the island growth mode does not.

Rocking curves give further information about the quality of the film. A narrow rocking curve indicates a good in-plane coherence (and a low density of dislocations).

In the following are some observations acquired during the search for the optimal growth conditions for overdoped $La_{2-x}Sr_xCuO_4$ films under tensile strain, on $SrLaGaO_4$ substrates. The starting point for this search was the ideal set of parameters for overdoped $La_{2-x}Sr_xCuO_4$ films under compressive strain. With these parameters we could already produce films that were epitaxially grown and exhibited tensile strain. With photoemission measurements it was not possible to detect any dispersion on such films.

Small changes in a parameter can already produce an effect on the film and therefore X-ray diffraction spectra have to be analyzed carefully.

An increase in the O_2 pressure does not affect the width of the rocking curve, but one can observe that finite size oscillations diminish in intensity until they vanish.

The same happens when the target-substrate distance is increased: the rocking curve remains narrow, but the finite size oscillations disappear.

Finite size oscillations can already be found at high substrate temperature (615 °C), but they are weaker and not frequent. When the temperature is lowered, they become more present. Also the rocking curves are narrow over a large temperature range. Photoemission measurements could only be done successfully on films grown at low substrate temperatures (550 °C).

Once the optimal growth parameters are found for films on $SrLaGaO_4$, they turned out to be the optimal parameters for films on $SrTiO_3$ too.

In table 3.1 the optimal growth parameters for two $La_{2-x}Sr_xCuO_4$ films are shown. L8464 is an overdoped film under compressive strain, on which ARPES measurements have been done. It represents at the same time the starting point for our search of the ideal conditions for the preparation of films under tensile strain. Such a film is 233LO on which ARPES measurements have been performed and are discussed in chapter 6.

Film	**L8464**	**233LO**
substrate	$SrLaAlO_4$	$SrTiO_3$
in-plane strain	compressive	tensile
doping	0.2 (overdoped)	0.2 (overdoped)
substrate temperature	613 °C	550 °C
oxygen pressure	300 mTorr	300 mTorr
distance between target and substrate	5cm	4 cm
laser power	146 mW	250 mW
pulsrate	2 pulses / s	3 pulses / s
c-axis	13.30 Å	13.10 Å

Table 3.1: Growth parameters for two overdoped $La_{1.8}Sr_{0.2}CuO_4$ *films, on which ARPES dispersion was observed*

For thin films (5 unit cells or less) under tensile strain, the rocking curves are in general very narrow. They have a FWHM (full width half maximum) of about 0.03° to 0.05° and are best fitted with a gaussian curve. Such a narrow rocking curve corresponds to the instrumental resolution and illustrates the excellent quality of our films (film 200LO in figure 3.1). The situation changes when the films become thicker. Then relaxation occurs and a large lorentzian contribution to the rocking curve can be distinguished, besides the gaussian contribution (film 210LO). When the film becomes very thick (22 unit cells), the rocking curve is dominated by the lorentzian contribution (film 199LO). The relaxation through dislocation leads to stacking faults, which give rise to the lorentzian form of the rocking curve.

The strain, one of the key properties of our films, was determined in the following way. In the θ-2θ scan the peaks of the film were identified and fitted, by a double gaussian, taking into acount the Cu-Kα1 and Cu-Kα2 contributions of the emitted X-rays. To correct a possible deviation between the c-axis of the film and the z-axis of the XRD-goniometer, the c-axis was calculated for each peak with Bragg's law:

$$2c\sin(\theta) = n\lambda \tag{3.1}$$

c is the c-axis length, n the order of the observed peak and λ the wavelength of the X-rays. Then the c-axis values from all the peaks were reported in a diagram depending on $\cos^2(\theta)/\sin(\theta)$. The crossing point with the y-axis gives the corrected c-axis [3.5].

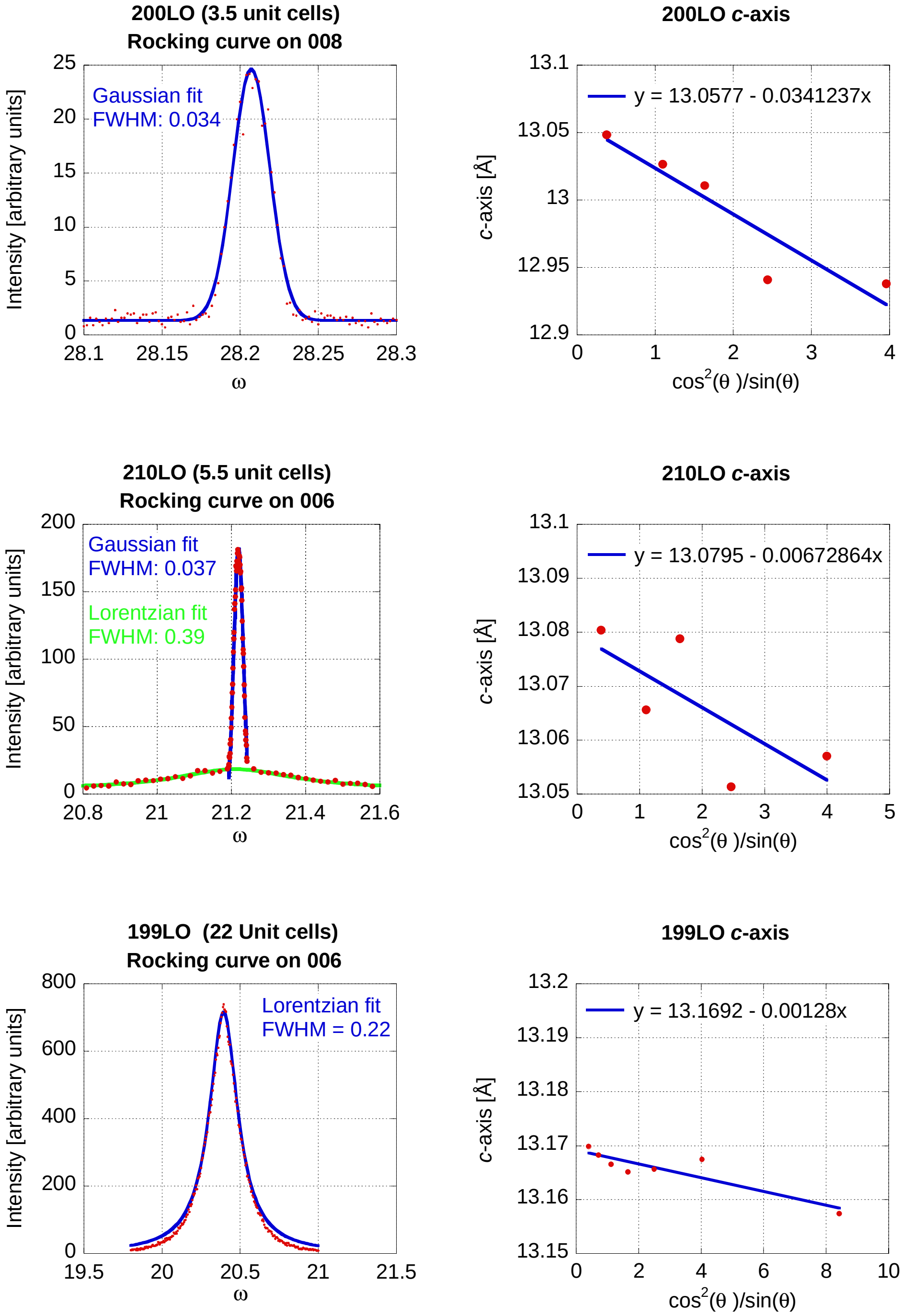

Figure 3.1: Rocking curve (left) and c-axis determination (right) for a film under tensile strain (13.06 Å) and two films under tensile strain that have partially relaxed (13.08 Å and 13.17 Å). The films are aligned along the c-axis and the rocking curves are measured at the peaks of order 8 (for 200LO) and 6 (for 210LO and 199LO).

In figure 3.1 one can see how the strain decreases when the film gets thicker. The thinnest film 200LO has a *c*-axis of 13.06 Å, the film that is partially relaxed 210LO has 13.08 Å and the most relaxed film 199LO has 13.17 Å. This is in agreement with the corresponding rocking curves.

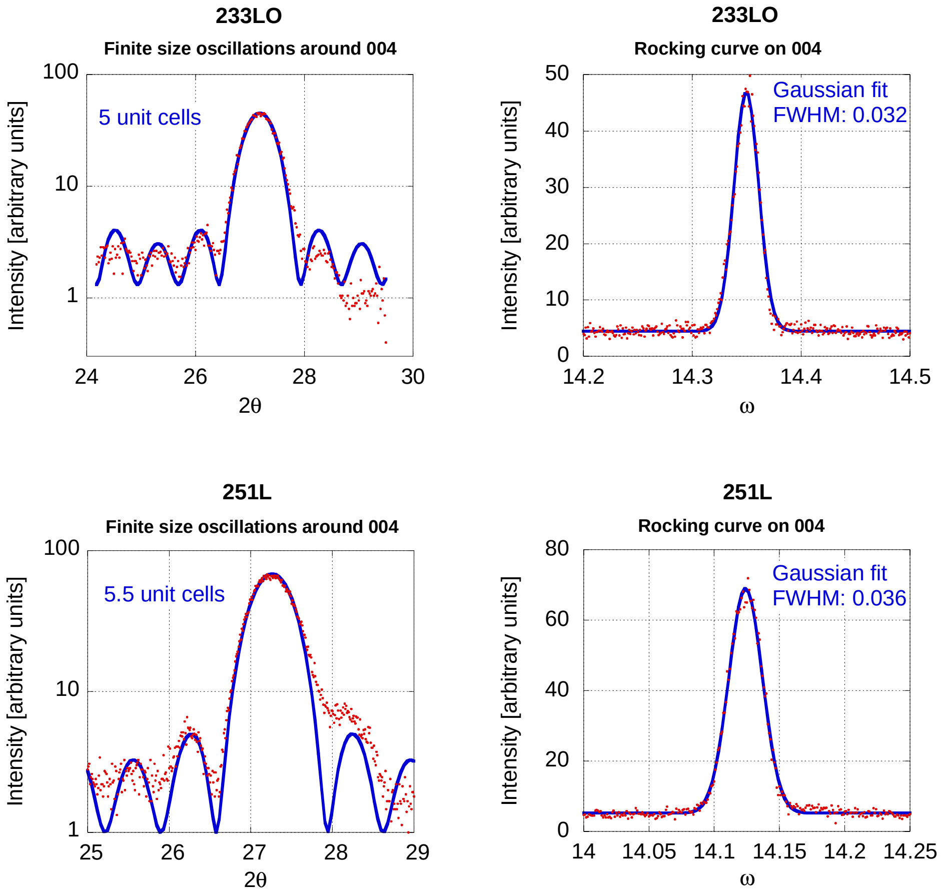

Figure 3.2: Finite size oscillations and rocking curves (on the peak of order 4, for samples aligned along the c-axis) from the films under tensile strain on which ARPES measurements have been performed.

The emergence of finite size oscillations is not only an indication for good surface quality, but they can also be used to estimate the film thickness by fitting them and adjusting the number of unit cells in the fit until it matches the measurement. An example is given in figure 3.2 with the films 233LO (overdoped) and 251L (optimally doped), which have been used for the ARPES measurements of chapter 6. They have a thickness of 5 and 5.5 unit cells. A half unit cell thickness can be measured, because the unit cell consists in two identical blocks that are just shifted one to the other.

The interplay of strain and doping in the film deserves some remarks. There are certain similarities between the application of strain through lattice mismatch and doping. Since the *Sr* atom is slightly bigger than the *La* atom, it induces also strain and the *c*-axis increases with the doping (for bulk crystals see tables in [3.7]). For $La_{2-x}Sr_xCuO_4$ films grown on a substrate with smaller *a*-axis ($SrLaAlO_4$) the following observation illustrates this fact: the bigger the *Sr* content, the smaller is the difference of the *c*-axis between a film under strain and a relaxed film. For overdoped films with a *Sr* content of $x = 0.22$ there is no difference anymore, the *c*-axis is the same for very thin and very thick films and cannot be changed through compressive in-plane strain (figure 3.3). As already mentioned in chapter 1, oxygen doping leads to intrinsic strain and to an expansion of the *c*-axis [3.8].

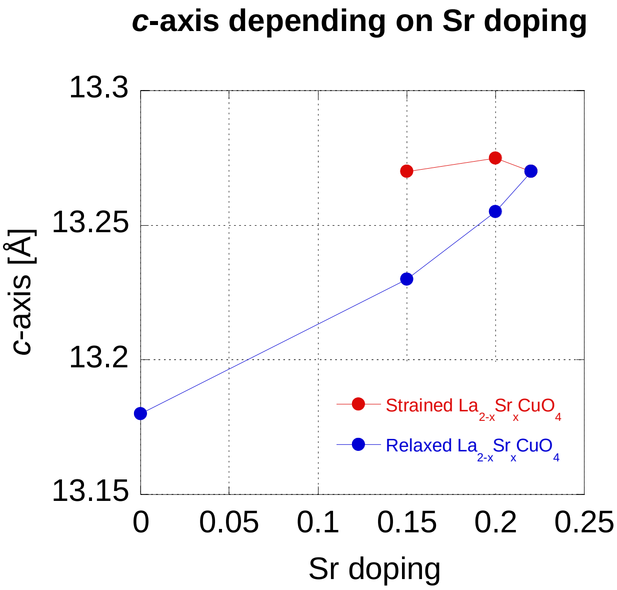

Figure 3.3: The difference between the c-axis of a compressively strained and a relaxed $La_{2-x}Sr_xCuO_4$ *film diminishes with increasing doping*

Chapter 4: ARPES Experiments and Analysis

Among all the measurement techniques that we use for the analysis of the properties of our samples, ARPES plays a central role. The fact that it is the most appropriate method for the determination of the electronic band structure makes it particularly interesting, because it can be compared in many cases to theoretical band structure calculations [4.1].
In this chapter I describe first how an ARPES experiment works and present the equipment we used. Then I introduce the three step model for the analysis of the measurements and finally explain the procedure that we developed to determine the electronic dispersion in various $La_{2-x}Sr_xCuO_4$ films. HTSC have normally a 2-dimensional band structure, which makes the ARPES interpretation much easier. In our measurements we have encountered samples with an electronic dispersion that cannot be explained within this two-dimensional frame. Therefore our method to determine the electronic band structure from the measurements is described in detail.
Figure 4.1 shows schematically how an ARPES measurement works. A photon source provides light in the ultraviolet or X-ray range. Through the photoeffect [4.2], the incident photons transmit their energy to the electrons of the sample, which are therefore ejected. An analyzer detects these electrons and records their kinetic energy and momentum.
Different photon sources can be used, we opted for synchrotron radiation [4.3]. The advantages of synchrotron light are the tunability of the photonenergy and the high brilliance of the light. Our ARPES measurements are performed at the Synchrotron Radiation Center in Madison. The beamline on which we measured has an undulator as insertion device and a 6m plane grating monochromator, which allows us to choose the photonenergy in the range between 8 and 245 eV. The sample is situated in an ultra high vacuum ($< 10^{-10}$ Torr) chamber, to keep its surface clean. It is mounted on a coldfinger and can be cooled down to 11 K. The electrons emitted from the sample by the synchrotron light are ejected in all directions. Those electrons, which are moving towards the analyzer are first retarded and focused by an electron lens system. Through the entrance slit, the analyzer accepts electrons with an incoming angle θ varying over 14°, corresponding to different momentum of the electron. The electrons are dispersed, depending on their kinetic energy, by a hemispherical electrostatic analyzer. Passing the exit slit, they reach finally the detector system, consisting in multi channel plates, a

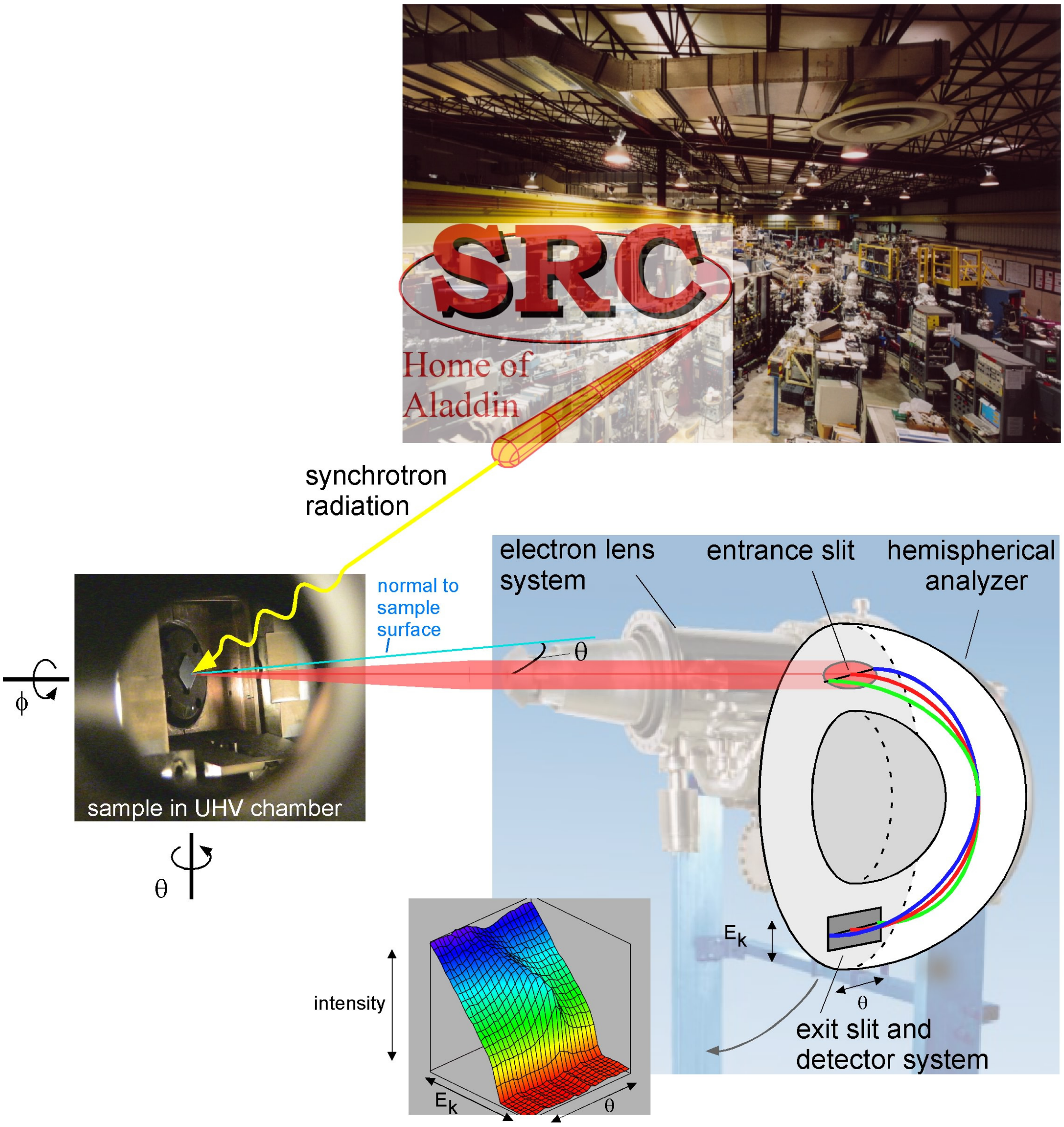

Figure 4.1: Sketch of an ARPES experiment. Synchrotron radiation from the SRC ejects electrons from the sample. Determined by the momentum, their paths (blue, red and green lines) have a different angle θ and enter the hemispherical chamber at different places. According to the kinetic energy, the electrons are dispersed in the hemispherical chamber. As a function of the energy and of θ they are recorded by a 2-dimensional detector system.

phosphor screen and a CCD camera. The detector system records the intensity of the arriving electron current as a function of the incoming angle θ and the kinetic energy.

The analyzers that we used for our measurements were a SCIENTA 200S and a SCIENTA SES 2002. On the SCIENTA 200S, with an energy resolution of 50 meV and a momentum resolution of ~0.08 Å^{-1}, we did the measurements on $La_{2-x}Sr_xCuO_4$ films under compressive strain. The measurements on $La_{2-x}Sr_xCuO_4$ films under tensile strain were performed on the SCIENTA SES 2002, with an energy resolution of 15 meV and a momentum resolution of 0.04 Å^{-1}.

The films were cooled to 11 K for the acquisition of the spectra presented in chapters 5 and 6. The lifetime of the samples was under such conditions of the order of 24 hours and the data acquisition time was about 30 to 60 minutes for a spectra.

4.1 Principles of ARPES

The following development is based on the books on photoemission written by Hüfner [4.4] and by Lynch and Olson [4.5]. [4.6] and [4.7] give an overview on Photoemission on HTSC.

The electronic structure is determined from ARPES measurements. The measured quantities are the kinetic energy E_k and the detection angle θ of the electron. The relations between these measured quantities and the initial state wave vector and binding energy E_B are deduced in what follows.

$\overrightarrow{k^{in}} = \overrightarrow{k_{//}^{in}} + \overrightarrow{k_{\perp}^{in}}$ is the wave vector of an electron in the initial state (before the absorption of a photon), with the component $\overrightarrow{k_{//}^{in}}$ parallel and $\overrightarrow{k_{\perp}^{in}}$ perpendicular to the sample surface. In ARPES $\overrightarrow{k_{//}^{in}}$ is conserved during the whole process under certain conditions that will be discussed later. This is a great advantage for the study of cuprates, since in *most* cases, there are no bands dispersing along the direction perpendicular to the CuO_2 planes and one does not have to care about $\overrightarrow{k_{\perp}^{in}}$.

If the third dimension has to be taken into account, the situation is more complex; $\overrightarrow{k_{\perp}}$ is not conserved, because the electron has to pass a potential energy step at the surface.

Inside the crystal it is exposed to the mean attractive inner potential V_0. A priori this potential is not known. There are several methods to determine it:

- it can be adjusted until the agreement between experimental and theoretical dispersion is optimal.
- the value of the theoretical "muffin-tin zero" can be used [4.4]
- one can look for symmetries in the experimental energy dispersion curves so that an observed period in the dispersion is in agreement with the size of the Brillouin zone

For our analysis we use the first method within the frame of the three step model [4.8] and the free-electron final state approximation.

The three step model is a phenomenological approach that splits the photoemission process into three steps. First the electron is excited by a photon from an initial state into a final state, then it travels through the sample to the surface and finally it escapes through the surface into the vacuum, where it is detected by the analyzer.

In the initial state, the electron has the wave vector $\overrightarrow{k^{in}} = \overrightarrow{k_{//}^{in}} + \overrightarrow{k_{\perp}^{in}}$ and its energy is the binding energy $E_{in} = E_B(\vec{k}) < 0$, measured with respect to the Fermi level.
From the initial state the electron is excited by a photon with energy $h\nu$ into the final state, still within the solid. Energy conservation requires for the final state energy E_{fin}, that:

$$h\nu = E_{fin} - E_{in} \tag{4.1}$$

Momentum conservation leads to the following relation for the wave vector

$$\overrightarrow{k^{fin}} = \overrightarrow{k_{//}^{fin}} + \overrightarrow{k_{\perp}^{fin}} = \overrightarrow{k^{in}} + \overrightarrow{k_{\gamma}} + \overrightarrow{G} \cong \overrightarrow{k^{in}} + \overrightarrow{G} \tag{4.2}$$

where $\overrightarrow{G}$ is a vector of the reciprocal lattice and $\overrightarrow{k_{\gamma}}$ is the wave vector of the photon. In materials with a 2-dimensional dispersion, it is the crystal recoil momentum that provides the necessary momentum to the electron along the perpendicular direction for its escape from the crystal and that leads to the term $\overrightarrow{G}$ in (4.2).

The wave vector of the photon $\overrightarrow{k_\gamma}$ is neglected, because it is very small at the energies that we use, thus in the reduced zone representation the transition is direct (figure 4.2). Transitions to the final state can only occur if such a state is available. The photon energy $h\nu$ has to be chosen so that it corresponds to the difference of the final state energy E_{fin} at the wave vector $\overrightarrow{k^{fin}} = \overrightarrow{k^{in}} + \overrightarrow{G}$ and the initial state energy E_{in}: $h\nu = E_{fin} - E_{in}$

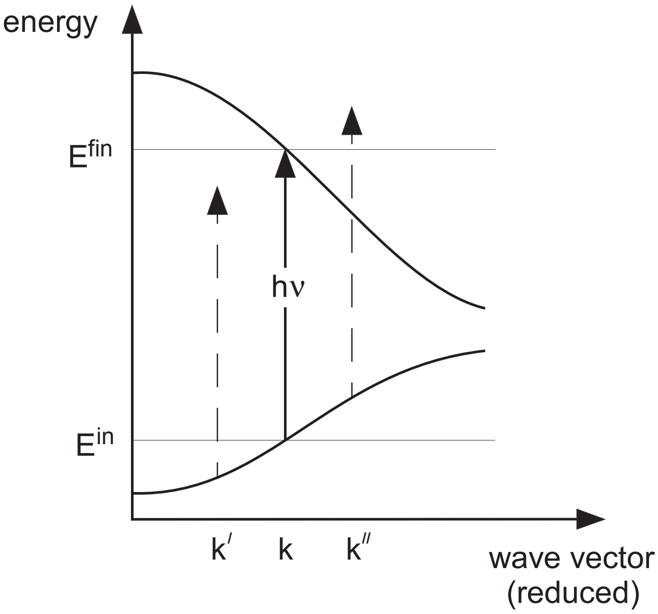

Figure 4.2: Transition between the initial state (E_{in}, $\overrightarrow{k^{in}}$) and the final state (E_{fin}, $\overrightarrow{k^{fin}}$). At photon energy $h\nu$ a transition is only possible at k, but not at k' or k".

In the free-electron final-state approximation it is assumed that a small periodic potential is present, so that $\overrightarrow{G}$ exists and that direct transitions in the reduced zone representation are possible. Nevertheless, the potential is so small, that the dispersion relation of a free electron can be taken for the final state:

$$E_{fin}(\overrightarrow{k^{fin}}) = \frac{\hbar^2}{2m*}(\overrightarrow{k^{fin}})^2 - |E_0| = E_B + h\nu \qquad (4.3)$$

In (4.3) m^* is the effective mass of the exited electron in the crystal. Often it is taken to be the free electron mass m. E_{fin} is measured with respect to the Fermi level, so $-|E_0|$ is the energy at the bottom of the band.

Once excited into the final state, the electron has to pass through the solid to the surface. Scattering, essentially due to electron-electron interaction, reduces the number of electrons that arrive at the surface. A so-called "universal curve" [4.9] gives the inelastic mean free path of the electron measured in elements (figure 4.3). For the cuprates this curve is expected to show a similar behavior. At photon energies between 20 and 70 eV, which we use for our ARPES measurements, the universal curve presents a minimum. The mean free path in this energy region is only of the order of several Angstroms or about one unit cell of $La_{2-x}Sr_xCuO_4$. The short mean free path limits the region of the sample that is probed by ARPES measurements to a few layers close to the surface.

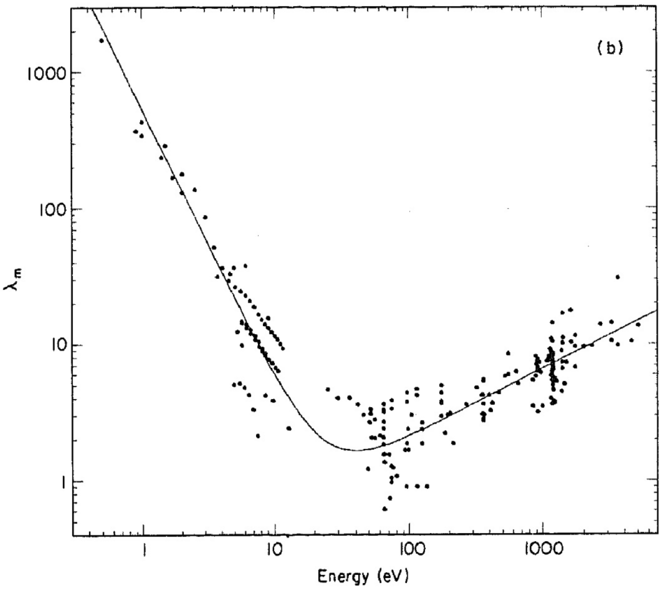

Figure 4.3: Inelastic mean free path (λ_m is the number of monolayers) of an electron in the sample (figure from [4.9])

To escape out of the solid into the vacuum, the electron has to overcome the surface potential barrier $V_0 = |E_0| + \phi$. The workfunction ϕ has its origin in the charge arrangement at the surface.

If the kinetic energy normal to the surface is insufficient, the electron will be reflected.

The wave vector in the vacuum is $\overrightarrow{k^{vac}} = \overrightarrow{k_{//}^{vac}} + \overrightarrow{k_{\perp}^{vac}}$.

Since the surface is an equipotential, there is no electric field component in the plane, thus $\overrightarrow{k_{//}^{fin}}$ is conserved.

$$\overrightarrow{k_{//}^{vac}} = \overrightarrow{k_{//}^{fin}} = \overrightarrow{k_{//}^{in}} + \overrightarrow{G_{//}} \qquad (4.4)$$

$\overrightarrow{G_{//}}$ is a vector of the reciprocal lattice, parallel to the surface. In our experiments, at a given photon energy, we choose θ so that $\overrightarrow{G_{//}}$ is zero for electrons from the first Brillouin zone.

For the perpendicular component there is no conservation. E_0 is a priori not known and $\overrightarrow{k_{\perp}^{fin}}$ cannot be easily determined (cf. figure 4.4).

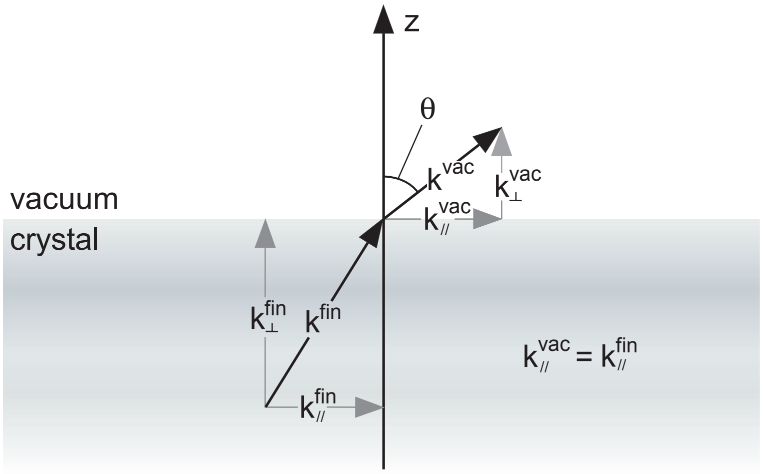

Figure 4.4: $\overrightarrow{k_{//}}$ *is conserved, but not* $\overrightarrow{k_{\perp}}$*, because the surface potential barrier has to be overcome*

The relation between the kinetic energy E_k and the wave vector is:

$$\left|\overrightarrow{k^{vac}}\right|^2 = \frac{2m}{\hbar^2}E_k \quad \Rightarrow \qquad k_{//}^{vac} = \sqrt{\frac{2m}{\hbar^2}E_k}\,\sin\theta \tag{4.5}$$

$$\text{and} \qquad k_{\perp}^{vac} = \sqrt{\frac{2m}{\hbar^2}E_k}\,\cos\theta \tag{4.6}$$

The kinetic energy is measured by the analyzer with respect to the vacuum, it is

$$E_k = h\nu - \phi + E_B \qquad \Rightarrow \qquad E_B = E_k - h\nu + \phi \tag{4.7}$$

To express $k_{\perp}^{in}$, we get from (4.3) and (4.7)

$$E_{fin} = E_k + \phi \quad \Rightarrow \quad \frac{\hbar^2}{2m^*}(\overrightarrow{k^{fin}})^2 - |E_0| = E_k + \phi \tag{4.8}$$

Together with (4.2), (4.4), (4.5) and (4.6) we can determine $\overrightarrow{k_{\perp}^{in}}$:

$$k_{\perp}^{in} = \sqrt{\frac{2m^*}{\hbar^2}}\sqrt{E_k(1-\frac{m}{m^*}\sin^2(\theta)) + \phi + |E_0|} - G_{\perp} \tag{4.9}$$

$G_{\perp}$ is a vector of the reciprocal lattice in the perpendicular direction.
(4.4) and (4.5) give $k_{//}^{in}$

$$k_{//}^{in} = \sqrt{\frac{2m}{\hbar^2}}\sqrt{E_k\sin^2(\theta)} \tag{4.10}$$

4.2 ARPES at Constant Photon Energy

From the above discussion, one can see that ARPES measurements, using *constant photon energy*, give dispersion curves $E_b(\overrightarrow{k^{in}})$ for $\overrightarrow{k^{in}}$ lying on a particular surface in the 3-dimensional reciprocal space defined by:

$$(k_{//}^{in})^2 + (k_{\perp}^{in} + G_{\perp})^2 = \frac{2m^*}{\hbar^2}(E_B + h\nu + |E_0|) \qquad (4.11)$$

For fixed binding energy $E_b = E$, (4.11) is the equation of a sphere centered at $(0, 0, -G_{\perp})$. In the following, we will call it the *constant photon energy probing sphere*. The probing sphere is located between two concentric spheres with slightly different radius:

$$(k_{//}^{in})^2 + (k_{\perp}^{in} + G_{\perp})^2 = \frac{2m^*}{\hbar^2}(h\nu) \qquad (4.12)$$

for the maximal binding energy (at the Γ point).

$$(k_{//}^{in})^2 + (k_{\perp}^{in} + G_{\perp})^2 = \frac{2m^*}{\hbar^2}(h\nu + |E_0|) \qquad (4.13)$$

for zero binding energy (Fermi level).

Each dispersion peak in the spectra corresponds to an initial state wave vector $\overrightarrow{k^{in}}$ belonging to the intersection of the probing sphere (4.11) – for the measured binding energy E – and the constant energy surface $E_b(\overrightarrow{k^{in}})$.

This intersection, for zero binding energy, when projected on the parallel plane (k_x, k_y) is the observed *Fermi contour*. When working with materials presenting a 2-dimensional dispersion, there is no $\overrightarrow{k_{\perp}^{in}}$ dependence on the binding energies. Fermi energy surfaces are then "vertical cylinders", and their intersection with any probing sphere gives always the same planar projection (Figure 4.5a). This is the reason why, in the literature, the Fermi contour is usually called the Fermi surface in the 2-dimensional case.

For materials with a 3-dimensional dispersion, the situation is quite different (Figure 4.5b): Fermi contours can display very tortuous shapes, varying from one photon energy to another, depending on the local topology of the Fermi surface at its intersection with the Fermi probing sphere (equation 4.13).

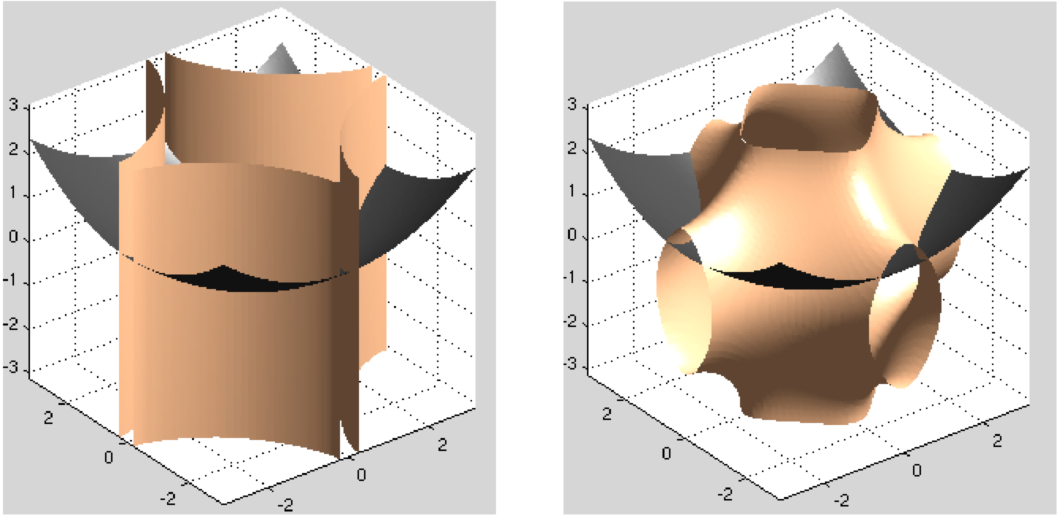

Figure 4.5: Intersections of the Fermi surface (light) with the black Fermi probing sphere for 2-dimensional (left) and 3-dimensional (right) dispersion.

4.3 Selection Rules

The measured ARPES intensity is proportional to the transition probability between the initial state and the final state, which is given by Fermi's golden rule

$$I \approx \frac{2\pi}{\hbar}\left|\left\langle \psi_{fin} \middle| \vec{A}\cdot\vec{p} \middle| \psi_{in} \right\rangle\right|^2 \delta(E_{fin} - E_{in} - \hbar\omega) \tag{4.14}$$

ψ_{in} and ψ_{fin} are the initial state and the final state wave functions, $\vec{A}$ is the vector potential of the photon and $\vec{p}$ is the momentum operator.

Symmetry constraints applied on the matrix element $\left\langle \psi_{fin} \middle| \vec{A}\cdot\vec{p} \middle| \psi_{in} \right\rangle$ lead to selection rules, which are explained in detail in [4.10]. A transition is allowed if the matrix element has an even symmetry. For a photon beam incident to a mirror plane of the sample, the final state ψ_{fin} must be even with respect to the mirror plane; otherwise it will not be discovered by the detector. If ψ_{fin} were odd, it would have a node in the mirror plane and therefore also on the detector axis.

When ψ_{in} is even, the polarization given by $\vec{A}$ has also to be even (parallel) with respect to the mirror plane. For an odd ψ_{in}, $\vec{A}$ has to be odd too.

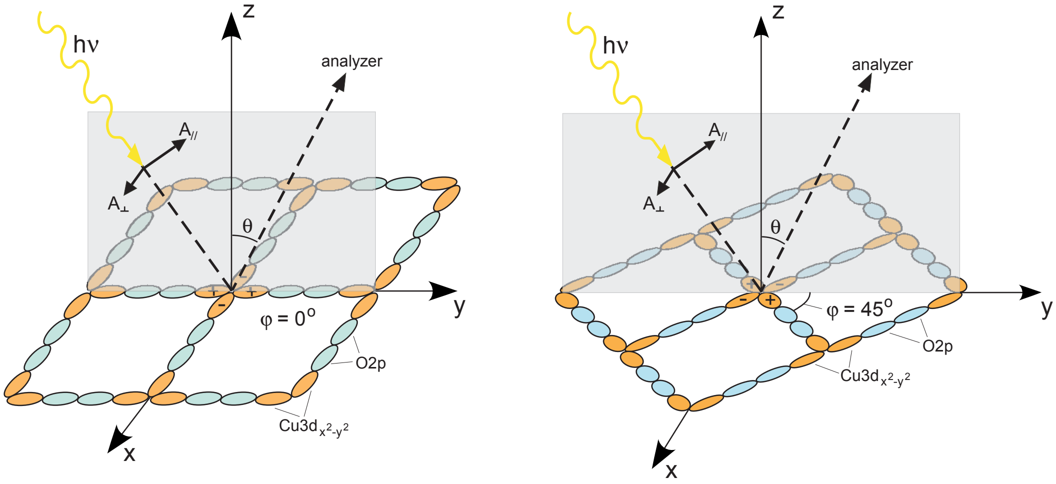

Figure 4.6: Selection rules due to the symmetry constraints influence the ARPES measurements. If the sample is oriented with $\varphi = 0°$ (beam arriving in the greyish mirror plane passing through the Cu-O bonds) ψ_{in} is even and $\vec{A}$ has to lay in the plane ($A_{//}$), otherwise the electrons will not be detected by the analyzer. To detect the electron for $\varphi = 45°$, where ψ_{in} is odd, $\vec{A}$ has to be odd too ($A_{\perp}$), with respect to the mirror plane.

Figure 4.6 illustrates this in the case of the CuO_2 plane. For a mirror plane perpendicular to the CuO_2 plane passing through the (0,0) – (π,0) direction, the symmetry of the $Cu3d_{x2\text{-}y2}$ orbitals hybridized with the *O2p* orbitals is even ("+" part of the orbital is reflected on "+" and the "–" on "–", see also figure 1.2). When $\vec{A}$ is parallel, then the transition is allowed and an ARPES signal can be measured. For a perpendicular $\vec{A}$ no intensity should be observed. When the mirror plane is oriented along the (0,0) – (π,π) direction the symmetry of the orbitals is odd and $\vec{A}$ has to be perpendicular to detect a signal.

4.4 Three-Dimensional Generic Tight Binding Approach

Here are presented the steps that we followed to establish our generic 3-dimensional tight binding model which is eventually used to fit the energy dispersion found with the ARPES measurements on $La_{2-x}Sr_xCuO_4$ films under tensile strain in chapter 6. The 2-dimensional restriction of this approach is employed in chapter 5 to fit the measurements on $La_{2-x}Sr_xCuO_4$ films under compressive strain.

We begin by writing the conduction band dispersion $E(\vec{k})$ as a truncated Fourier series, since it has the periodicity of the reciprocal lattice. The dispersion $E(\vec{k})$ becomes:

$$E\left(\vec{k}\right) = \sum_{n_a, n_b} E_{n_a, n_b} \exp\left[\ i\vec{k} \cdot \left(n_a \vec{a} + n_b \vec{b}\right)\ \right] \tag{4.15}$$

and

$$E\left(\vec{k}\right) = \sum_{n_a, n_b, n_c} E_{n_a, n_b, n_c} \exp\left[\ i\vec{k} \cdot \left(n_a \vec{a} + n_b \vec{b} + n_c \vec{c}\right)\ \right] \tag{4.16}$$

for 2 and 3 dimensions respectively. $\vec{k}$ is the wave-vector of the electron in the conduction band, (n_a, n_b, n_c) are integers specifying the harmonic's order for each direction, ($\vec{a}, \vec{b}, \vec{c}$) are the lattice constants in the direct space. The simplest approximation consists of retaining just terms up to the first harmonic, i.e. $n_i = 0$ and ± 1. Using the fact that $E(\vec{k})$ is an even function in the $\vec{k}$ variable, only cosine functions will enter into the expression of $E(\vec{k})$.

Using, in addition, the tetragonal symmetry of the $La_{2-x}Sr_xCuO_4$ unit cell (a = b and identical dispersion along x and y directions), the leading terms can be rearranged and the expression in 2 dimensions reduces to:

$$E\left(\vec{k}\right) \approx E_{0,0} + 2E_{1,0}\left[\cos(k_x a) + \cos(k_y a)\right] + 4E_{1,1}\cos(k_x a)\cos(k_y a) \tag{4.17}$$

This development is not based on a microscopic model, the energy is simply written as a Fourier series. Nevertheless, by renaming the coefficients, we find the 2-dimensional tight binding approximation:

$$E(\vec{k}) = \mu - 2t(\cos(k_x a) + \cos(k_y b)) + 4t'\cos(k_x a)\cos(k_y b) \tag{4.18}$$

In terms of the tight binding approximation *t* and *t'* correspond to the hopping probabilities from a site to its nearest neighbor (*t*) and to its next nearest neighbor (*t'*), μ is the chemical potential. The parameters *t*, *t'* and μ have the dimension of an energy.

In three dimensions the energy dispersion in terms of a Fourier series, truncated after the first harmonic becomes:

$$\begin{aligned} E\left(\vec{k}\right) \approx\; & E_{0,0,0} + 2E_{1,0,0}\left[\cos(k_x a) + \cos(k_y a)\right] + 2E_{0,0,1}\cos(k_z c) \\ & + 4E_{1,1,0}\cos(k_x a)\cos(k_y a) + 4E_{1,0,1}\left[\cos(k_x a) + \cos(k_y a)\right]\cos(k_z c) \\ & + 8E_{1,1,1}\cos(k_x a)\cos(k_y a)\cos(k_z c) \end{aligned} \tag{4.19}$$

A formulation in terms of k_z dependent hopping terms *t* and *t'* can be used to put in evidence the 2-dimensional tight binding restriction in the tetragonal symmetry:

$$E\left(\vec{k}\right) = \mu(k_z) - 2t(k_z)\left[\cos(k_x a) + \cos(k_y a)\right] + 4t'(k_z)\cos(k_x a)\cos(k_y a) \tag{4.20}$$

where

$$\begin{gathered} \mu(k_z) = E_{0,0,0} + 2E_{0,0,1}\cos(k_z c), \\ t(k_z) = -\left(E_{1,0,0} + 2E_{1,0,1}\cos(k_z c)\right) \quad \text{and} \quad t'(k_z) = \left(E_{1,1,0} + 2E_{1,1,1}\cos(k_z c)\right) \end{gathered} \tag{4.21}$$

Indeed, for a fixed k_z, the dispersion in the (k_x, k_y) plane takes the familiar form of the 2-dimensional tight binding approximation with nearest and next-nearest neighbors hopping terms *t* and *t'*. The k_z dependent "chemical potential" μ fixes the position of the band as a function of k_z, but it can be arbitrarily shifted, depending on the choice of the energy axis.

Let's now introduce a further approximation in (4.20), based on the usual interpretation of the hopping probabilities *t* and *t'* as overlap integrals between the considered atomic orbitals: The ratio $r = t'/t$ characterizing the relative in-plane hopping probabilities can be considered as a k_z independent quantity. Under these conditions, expression (4.20) becomes:

$$E(\vec{k}) \approx C + t(1 - \nu \cos(k_z c))\{\mu - 2(\cos(k_x a) + \cos(k_y a)) + 4r \cos(k_x a)\cos(k_y a)\} \quad (4.22)$$

with the following identities:

$$C = E_{0,0,0} + \frac{E_{0,0,1} \cdot E_{1,0,0}}{E_{1,0,1}}; \qquad t = -E_{1,0,0}; \qquad r = -\frac{E_{110}}{E_{100}};$$

$$\nu = -2\frac{E_{1,0,1}}{E_{1,0,0}} \quad \text{and} \quad \mu = -2\frac{E_{0,0,1}}{E_{1,0,1}} \quad (4.23)$$

Since we are interested in the binding energy $E_B(\vec{k}) = E(\vec{k}) - E_F$, the energy axis is chosen in order to absorb the constant C. The generic expression for the *tetragonal 3-dimensional band structure* is finally:

$$E_B(\vec{k}) = t[1 - \nu \cos(k_z c)]\{\mu - 2(\cos(k_x a) + \cos(k_y a)) + 4r \cos(k_x a)\cos(k_y a)\} - E_F \quad (4.24)$$

Expression (4.24) is simply the 2-dimensional tight binding expression periodically modulated by the z-axis dispersion factor $[1 - \nu\cos(k_z c)]$. In addition to t, t' (or r) and μ, there is now one more parameter (ν) compared to the case of 2 dimensions.

The relative k_z dispersion is controlled by ν, while r and t are respectively related to the shape of the in-plane 2-dimensional restriction and to the total bandwidth.

4.5 Fitting the ARPES Data

The ARPES measurements were performed along the two high symmetry directions $\Gamma - \mathrm{X}$ (φ = 0°), $\Gamma - \mathrm{M}$ (φ = 45°) and for a few other selected φ angles (figure 4.7). The θ angles have been varied in a large region around the Fermi surface, often over the whole first Brillouin zone. Measurements were performed at one or two different photon energies, for which it was possible to observe a dispersion.

With hindsight we would have put more weight on ARPES measurements at different photon energies in order to map the 3-dimensional Fermi surface of our samples.

Given the 2-dimensional character in the Fermi surfaces of most HTSC, we did not expect such a huge contribution of the third dimension.

In figure 4.7 the grey circles determine, where the band crosses the Fermi surface. The black line passing through the grey circles is the Fermi contour for a fixed photon energy, i.e. a cut through the 3-dimensional Fermi surface (cf. figure 4.5).

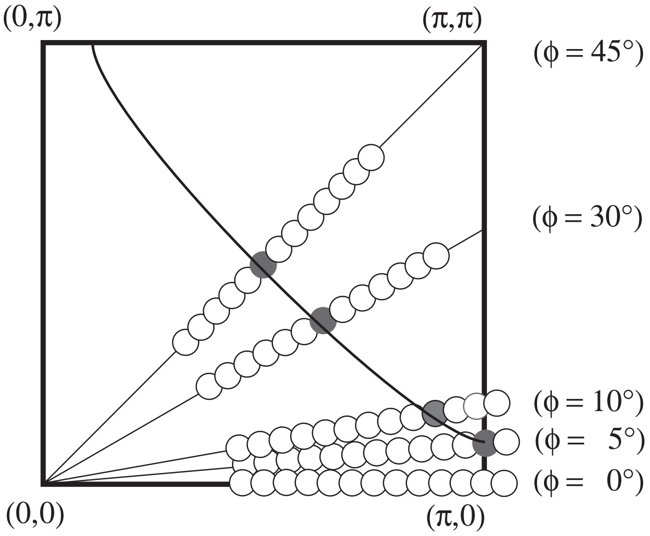

Figure 4.7: Typical measured θ and φ angles, grey circles show where the conduction band crosses the Fermi surface

To fit the energy dispersion of our data we use equation (4.24), in which we introduce (4.9) and (4.10) to express the wavevector. There are now 6 parameters to determine: t, t' (or r), μ, ν, E_0 and m^*. As the doping of our films is known, there is also one more constraint to be respected, the Luttinger rule [4.11]:

The fraction of the volume enclosed by the Fermi surface in the first Brillouin zone gives the filling of the band.

In the case of $La_{2-x}Sr_xCuO_4$ the number of electrons per site n is $0 < n < 2$. For undoped $La_{2-x}Sr_xCuO_4$ with $x = 0$, i.e. for La_2CuO_4, there is one electron per site and $n = 1$. For increasing hole doping x, n is decreasing. The relation between the size of the Fermi surface V_{FS}, n and x is:

$$V_{FS} = \frac{1}{2} n \cdot V_{BZ} = \frac{1}{2}(1-x) \cdot V_{BZ} \tag{4.25}$$

V_{BZ} is the volume of the Brillouin zone. Through the Luttinger rule we can relate r, t, μ and E_F, so that there are 5 free parameters left.

In practice the fit is done in the following way: The energy dispersion is fitted with one set of parameters for the different φ angles. The parameters are adjusted until an optimal agreement is reached. Obviously if high quality ARPES beamtime were readily available, we would have measured the Fermi surface in more detail, which would somewhat strengthen this procedure.

To determine the energy dispersion and the Fermi surface in our films we make several simplifying assumptions.

For the electronic structure we write the energy dispersion as a Fourier series that we truncate after the first harmonic. One could consider more terms of the Fourier series or even use a microscopic model to describe the energy dispersion. However we expect already an acceptable agreement for our simple approximation, yet it must be decided by comparing the fitted curve with the measurements, whether additional terms should be included.

The three step model, as it is presented here, is an independent electron model, where each measured photoelectron corresponds to an initial independent electron state. The reaction of other electrons to the remaining hole is not taken into account. While the model can be used rather successfully for nearly free-electron metals, it may seem inadequate for HTSC and related materials, where electron correlations are present. Correlations may explain the broadening of the peaks observed in our data. Nevertheless, it is the most commonly used model for the interpretation of photoemission spectra and it turned out to be quite successful.

To determine the final state wave vector we made the free electron final state approximation. This approximation gets better for higher photon energies, because the effect of the potential becomes weaker when the kinetic energy increases.

Justification for the free electron final state approximation as well as for the three step model in general is found in the fact, that they have been used very successfully for the interpretation of numerous experiments by many groups worldwide [4.4]. The good results together with the convenience and the comprehensibility make them a standard tool for the interpretation of ARPES measurements.

These methods can be further refined or other more elaborated models can be applied. Instead of the free electron final state approximation, one can take final states derived from band structure calculations using the local density approximation. In order to lower the effort that has to be done for data evaluation, hybrid methods are used, where the calculated bands are approximated with a free electron parabola.

An absolute determination without any previous assumptions would be an ideal way to derive band structures. Several methods exist [see 4.4], yet they are all quite complex and require a huge experimental effort and more ARPES beamtime.

Electron-electron interaction can be taken into account in our analysis by substituting the delta function in (4.14) with the spectral function of the electron. Such a treatment leads to a change in the expected photoemission spectra. Where a spectrum from a non-interacting system shows a unique peak with binding energy E_B, the corresponding spectra for an interacting system shows a main peak with a tail at higher binding energies, due to internal excitations of the system.

Despite its success the three step model has some weaknesses and can impair an advanced interpretation of the ARPES measurements. It does not take into account the surface photoeffect or any surface specific effects. Since the mean free path is very short, the signal from the surface becomes important in the measured spectra.

The distinction of three steps is artificial and for a small mean free path the transport to the surface and the escape into vacuum cannot be separated.

For all these reasons the more sophisticated one-step model has been elaborated [4.4, 4.5]. It does not divide the photoemission process into steps and is better suited for effects of electron interaction on the ARPES spectra, as well as for the evaluation of photoemission intensities from ab-initio band structure calculations.

However, because of the success of the three step model, we use it to guide us in our experiments and do not take into account correlation effects during the photoemission process. On the basis of the results of this first approach, more advanced methods and models can be implemented.

Chapter 5: ARPES Measurements on $La_{2-x}Sr_xCuO_4$ Films under Compressive Strain

Our investigations on $La_{2-x}Sr_xCuO_4$ began with films grown on $SrLaAlO_4$ substrates, hence exposed to in-plane compressive strain. The two first years of this thesis, my work was concentrated on such films and ARPES measurements to determine their electronic structure.

Typical $La_{2-x}Sr_xCuO_4$ films under compressive strain, appropriate for ARPES measurements, were produced following the procedure described in chapter 3. Their thickness is typically ~100 Å (about 8 unit cells). For the analysis of the ARPES measurements, we used the methods developed in chapter 4, for the case of a 2-dimensional dispersion.

The results of these measurements have been published in [5.1] and much more elaborated in a previous thesis [5.2]. These results served us for orientation and as a starting point in our research work on films under tensile strain.

Here is an extract from [5.1] as a summary of the results:

> “In-plane compressive strain is known to increase the critical temperature (T_C) of high temperature superconductors (HTSC). This phenomenon is quite dramatic [5.3, 5.4] in $La_{2-x}Sr_xCuO_{4-\delta}$ (LSCO) thin epitaxial films: for $x = 0.1$, T_C doubles with respect to relaxed LSCO (and increases by a factor of 5 with respect to films with in-plane tensile strain [5.4]). The published theoretical electronic band structure calculations [5.5, 5.6] predict the in-plane compressive strain to flatten the bands. This could provide a simple explanation for the dramatic T_C increase, since band flattening implies an enhanced density of states near the Fermi energy E_F. Our angle-resolved photoemission spectroscopy (ARPES) studies on strained LSCO films flatly contradict this picture by revealing a dispersing band that crosses E_F. This experimental result thus directly impacts the models dealing with the influence of pressure on superconducting properties [5.5-5.9]. The justification of strain effects must be sought beyond the band flattening framework of mean field models [5.10, 5.11]. Consequently strained HTSC

films have been studied rather extensively because of the spectacular strain effects on T_C [5.3, 5.4]. So far, however, the corresponding electronic structure changes had not been probed directly. We used ARPES to fill this gap by studying in situ grown LSCO films. This, incidentally, is the first direct ARPES study of as-grown HTSC films (as opposed to cleaved or scraped bulk samples [5.12] and/or cleaved thin films [5.13]). [...]

The samples have been characterized as described in chapter 3 and in [5.14, 5,15]. [...]

Following ARPES measurements, X-ray diffraction (XRD) was performed on each sample to measure its strain. Upon refinement of the X-ray diffraction data along the (001) direction on maximally strained films, we consistently obtained for both OPT (x = 0.15) and OD (x = 0.20) samples c = 13.29 ± 0.02 Å for the c-axis and d_{AP} = 2.50 Å for the Cu-O apical distance, in agreement with Ref. [5.4]. In comparison with the relaxed bulk values (c = 13.23 Å; d_{AP} = 2.43 Å) this corresponds to a change of +0.60 % for the c-axis and + 2.9 % for d_{AP}.

Figure 5.1(a) shows photoemission spectra for an OPT strained film, plotted as momentum distribution curves (MDC), taken at 6.5 K along the reciprocal space $\Gamma - X$ direction [(0, 0) to (π/a, 0)]. The MDC representation provides a much clearer picture than the energy distribution curves (EDC) when a band approaches the Fermi edge cutoff [5.16]. The MDC in figure 5.1(a) clearly show a peak moving towards E_F and crossing it at k_x = 0.82 π/a. A similar crossing was observed in strained UD (x = 0.10) samples. These experimental findings are very different from the previously obtained results [5.17] on scraped (unstrained) single crystals that show no E_F crossing except for highly overdoped samples (x > 0.22).

figure 5.1(b) illustrates the MDC dispersion for the same OPT strained films along the $\Gamma - M$ direction. The E_F crossing occurs at $k_x = k_y$ = 0.42 π/a, well beyond the crossing point ($k_x = k_y$ = 0.37 π/a) reported in Ref. [5.17] for OPT single-crystal samples. This indicates that additional occupied states in strained films close to (π/2a, π/2a) balance the disappearance of those related to the saddle point (0, π/a) in unstrained samples

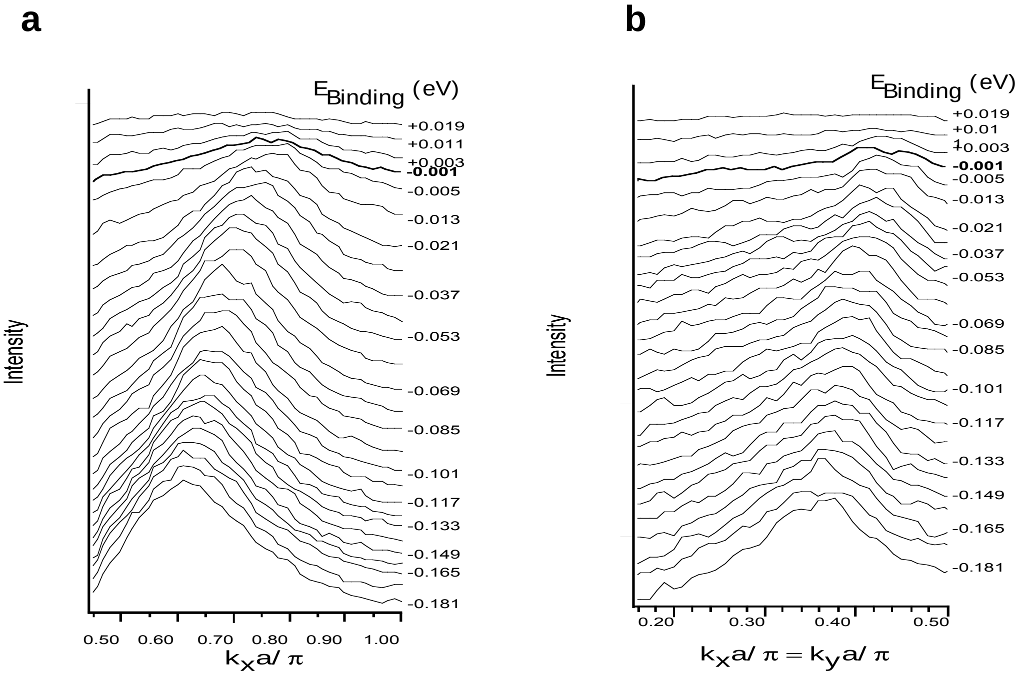

Figure 5.1: (a) Angle-resolved MDC ARPES data along the $\Gamma-X$ direction for an optimally doped (x = 0.15) LSCO film under in-plane compressive strain. (b) Angle-resolved MDC ARPES data along the $\Gamma-M$ direction for the same sample as in (a).

consistent with equal doping (x = 0.15) in both cases. T_C of our strained films is 44 K, 6° higher than for relaxed films, consistent with the already known effects of compressive strain on T_C [5.4]. Specifically, this also rules out the possibility of accidental overdoping as an explanation of the observed closed Fermi contour.

In figure 5.2(a), we plot band dispersions of the OPT strained film (circles) and the bulk sample (squares, Ref. [5.17]), along $\Gamma-$X and $\Gamma-$M, the latter projected on the k_x axis. The points correspond to the intensity maxima in our thin-film MDC and in the EDC of Ref. [5.17]. Contrary to the E_F crossing in strained films, the unstrained data along $\Gamma-$X reveal a saddle point remaining at least 0.025 eV below E_F. [...]

Equation (4.20) was used to fit the data of figure 5.2(a) with the constant doping level constraint x = 0.15. This constraint was implemented by noting that μ is related to the band filling n, and therefore to the hole

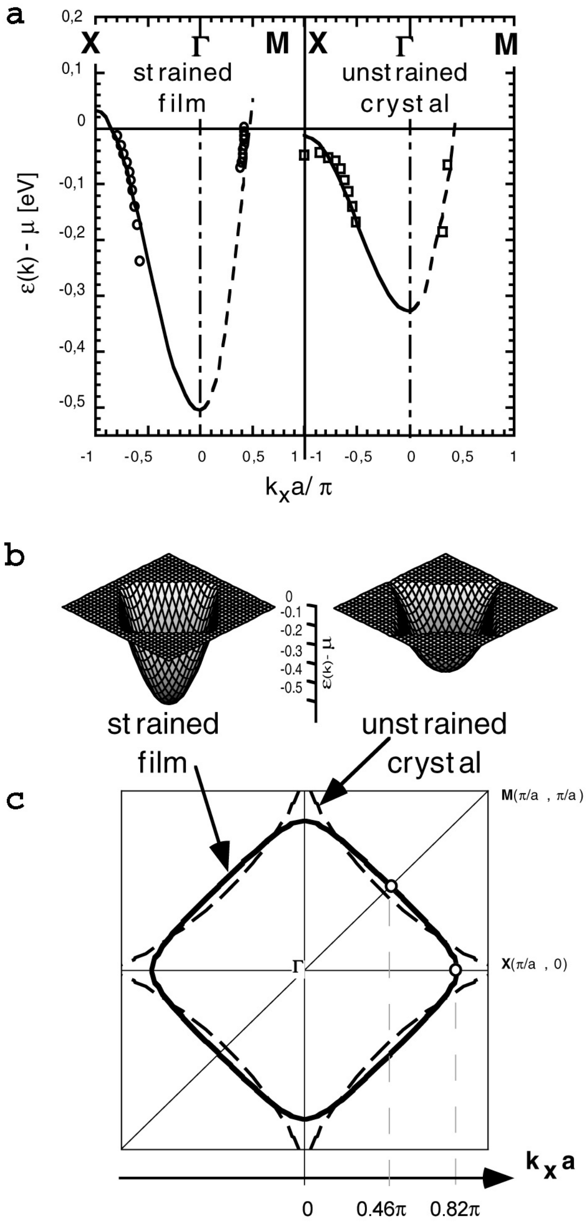

Figure 5.2: (a) Fits of band dispersion for a strained film (circles, left panel) and for an unstrained single crystal (squares, right panel, data from Ref. [5.17]), along $\Gamma - X$ (solid line) and $\Gamma - M$ (dashed line). The fits are based on equation 4.20. (b) Visualization of the best-fit results: dispersion of the two-dimensional band for an optimally doped in-plane compressed film (left) and for an unstrained optimally doped single crystal (right). (c) Schematic illustration of changes in the Fermi surface topology.

doping level $x = 1\text{-}n$. We choose μ so that the area enclosed by the Fermi surface (FS) is $n = 0.85$. The best-fitting parameters are $t = 0.135$ eV and $t' = 0.028$ eV for the unstrained crystal (Ref. [5.17]) and $t = 0.145$ eV and $t' = 0.005$ eV for the strained film (the uncertainty on t and t' is 0.002 eV). Thus, $r = t'/t$, the parameter characterizing the band shape, equals 0.21 for the unstrained crystal and 0.036 for the strained film. Main changes in the dispersion derived from the best fit are illustrated in figures 5.2(b) and 5.2(c). The strong reduction of r by a factor of 5 enhances the band dispersion and distorts the FS. The FS (figure 5.2(c)) is shifted inwards along $\Gamma-\mathrm{X}$ and outwards along $\Gamma-\mathrm{M}$, changing its topology from holelike to electronlike. The vanishing of the saddle point is illustrated in figure 5.2(b). The NN hopping term t slightly increases in the strained sample; this is reasonable since a small in-plane lattice contraction enhances the overlap integrals between the NN $Cu\ 3d_{xy}$ and $O\ 2p_x$ orbitals. The same trend should be expected for the NNN hopping t' (overlap between the $O\ 2p_x$ and $O\ 2p_y$ orbitals). In fact, the increase should be much stronger for t' than for t since the NNN overlaps are much weaker [5.6]. Surprisingly, the observed trend is exactly the opposite: the NNN hopping t' is much lower for strained films than for the unstrained sample. This fact is not accounted for by published theoretical models [5.5, 5.6]. Note that our X-ray diffraction data show that the strain induced changes are much bigger for the *Cu-O* apical bond than for the other interatomic distances. This suggests a change in coordination and therefore in the hopping integrals that cannot be properly described by those theoretical models [5.5, 5.6] that assume a rigid lattice and no coordination changes.

In substrate mismatched epitaxial films, when elastic energy is relaxed, it does so via misfit dislocations resulting in poor quality film surfaces. As a consequence, in relaxed optimally doped films, the significant incoherent background in ARPES prevented us from extracting the dispersion. This is a sensitive point, since the previous comparison between bulk and film samples was built on the assumption that film and bulk surfaces have no inherent differences (except for the strain). However, since band features become stronger with doping, in the OD regime ($x = 0.20$), we have

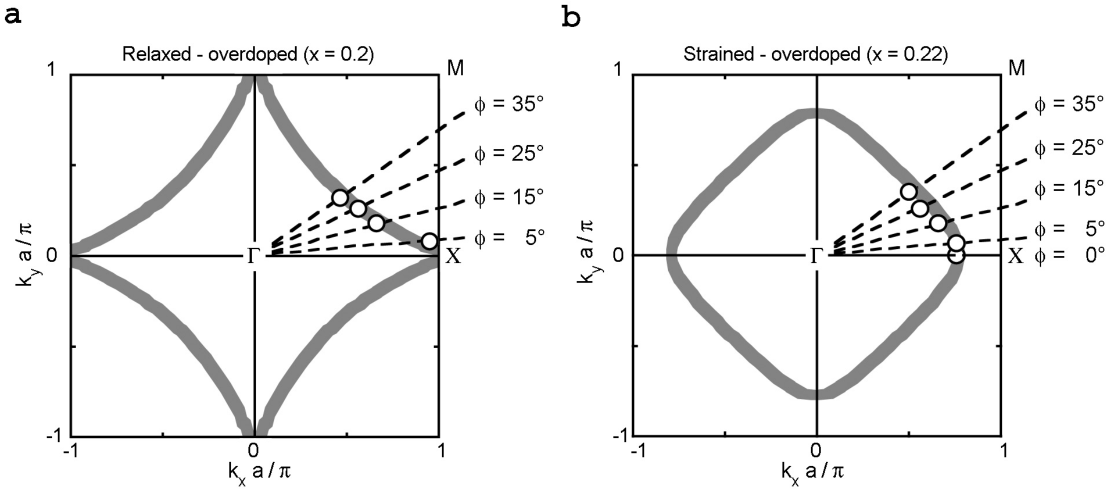

Figure 5.3: Fermi surfaces of relaxed (a) and strained (b) overdoped films. White dots are located at the observed crossing points. Thick grey lines are calculated within the tight-binding approach (Eq. (4.20)), for x = 0.20. The size of the circles corresponds to the estimated error (±0.1).

measured the dispersions of both relaxed and strained films. The 2D FS in figure 5.3(a) is that of an OD relaxed film with a superconducting T_C of 24 K. Dashed lines indicate the scan directions in *k* space, and the white dots are located at the intersection of the band with E_F, observed on MDC plots. The thick grey line is calculated with Eq. (4.20), using the constraint $x = 0.20$ and the band parameters $t = 0.135$ eV and $t' = 0.036$ eV, very close (20%) to those found for the relaxed bulk. Similarly, in figure 5.3(b), we show the FS of an OD strained film with a superconducting T_C of 40 K (film L8464 from table 3.1). The band parameters used to draw the thick grey line are $t = 0.145$ eV and $t' = 0.0052$ eV, the same as for the optimally doped strained film. The agreement is not surprising since the XRD analysis shows almost the same strain ($c = 13.30 \pm 0.02$ Å) as for the OPT film. Thus the effect of strain on band structure, observed for OPT LSCO films is unambiguously confirmed, qualitatively and quantitatively, in the OD case. Moreover, the influence of inherent differences between bulk and film surfaces can be discarded. Indeed, the results obtained on the relaxed OD LSCO film are the same as for the bulk OD single-crystal reported in Ref. [5.17].

> In summary, we have performed direct ARPES measurements on UD, OPT, and OD strained LSCO films and have measured a dispersing electronic band that crosses E_F well before the Brillouin zone boundary, in contrast to a flat band observed in both unstrained films and single crystals [5.17]. Our results rule out a simple explanation of the strain-induced changes in T_C based on the increase in the density of states near E_F [5.18 - 5.20]. The fact remains that in-plane compressive strain does increase the critical temperature as confirmed by our measurements. Our findings, therefore, have a general impact on the evolving theories of high temperature superconductivity. [...]"

Reactions to this article were numerous, especially from theorists [5.21]. The main criticisms were about our fit and about the oxygen content that was suspected to change under strain.

In our approach, the band dispersion is approximated as a truncated Fourier series (see chapter 4). If necessary for precision, it can be expanded to higher harmonic terms. There is no a priori underlying physical model. Just by analogy to the tight binding approach, *t* and *t'* are roughly interpreted as hopping terms and our approach is called "generic tight binding approach".

The Emery model is used in [5.21] to fit our data. It is an extended Hubbard model in which the pairing is mediated by strong coupling to local spin configurations on the *Cu* sites [5.22, 5.23]. However, it is not able to fit our data to a better agreement than the generic tight binding approach (see figure 1 in [5.21]). Thus a more comprehensive model built on a more solid theoretical basis is needed to account for the measured dispersion.

The second critical argument, the oxygen content of our films, is a sensitive point, since the oxygen content is not precisely known in our films. The influence of additional interstitial oxygen in $La_{2-x}Sr_xCuO_{4+\delta}$ thin films was studied in detail by Bozovic et al. [5.24]. With their optimized annealing procedure they achieve a T_C of 40 K in $La_2CuO_{4+\delta}$ films grown on $SrTiO_3$ substrates and 48 K on $SrLaAlO_4$. However, they write that the increase in T_C is much smaller in optimally doped and overdoped $La_{2-x}Sr_xCuO_{4+\delta}$. Intuitively one expects this, since at optimal doping, further doping with oxygen should not increase the T_C.

For an optimally doped film, where T_C is measured once after an annealing in vacuum and once after their optimized annealing procedure, they get a difference in T_C of about 4 K (see figure (3b) in [5.24]). For overdoped films the influence of interstitial oxygen is even smaller.

Interstitial oxygen does not only add holes, but it increases at the same time the *c*-axis (Bozovic et al. report a *c*-axis of 13.29 Å in $La_2CuO_{4+\delta}$ films on $SrTiO_3$ and up to 13.26 Å on $SrLaAlO_4$). Therefore not only the doping, but also the strain affects T_C and it is not clear which effect is dominant.

Our annealing at 1 bar in O_2, must have much less effects than their optimized annealing procedure in ozone (with an effective oxidation power corresponding to 200 bar O_2). For that reason, we do not expect that interstitial oxygen plays an important role in our films (in accordance with [5.25]). Especially the T_C enhancement in our overdoped film from 24 K to 40 K under compressive strain cannot be explained by interstitial oxygen.

With regard to measurements on films under tensile strain, we noticed the following points:

- the generic tight binding approach proved to be very useful for the analysis of our ARPES measurements.
- for films under compressive strain, the overdoped films show the best signal to noise ratio in ARPES measurements, whereas the underdoped films are most difficult to measure.

In addition to the ARPES studies, we have established several ongoing collaborations on complementary measurements on our $La_{2-x}Sr_xCuO_4$ films under compressive strain with other groups worldwide. This work is still in progress, so here I just give a brief outline on the preliminary results and discussions.

In order to determine the exact changes of lattice coordination with strain we have begun a collaboration with S. Conradson and coworkers (Los Alamos National Laboratory) on EXAFS studies on our films. The preliminary data indicate that indeed there are numerous subtle changes to the lattice under the strain, yet to establish the exact correlations with T_C, and with the normal and superconducting state properties, more samples have to be studied systematically.

However, the early data indicate that the samples tend to be more homogeneous in the superconducting state than in the normal state, i.e. that there are even some changes when the films are cooled below the superconducting transition.
Moreover, the preliminary reflectivity measurements on our films by S. Sinha and coworkers (University of California, San Diego) also indicate that, when temperature is lowered below T_C, there is a change in reflectivity, which means a change in the electron density distribution.

These joint efforts together with planned Raman studies in collaboration with H.-U. Habermeier (Max Planck Institute in Stuttgart), when completed, should eventually provide important insights into the subtle changes of the ionic correlations, electronic structure and properties of strained films (as compared to relaxed films or to bulk crystals). It is clear and all the aforementioned groups agree that the lattice strain plays a very important role in HTSC cuprates [5.26, 5.27] and that these effects cannot be accounted for within simple (rigid lattice, mean field) models that presently dominate the theorists' discussions. A. Bussmann-Holder (Max Planck Institute in Stuttgart) is doing calculations, which seem to be in accordance with the picture derived from our measurements [5.28].

Chapter 6: ARPES Measurements on $La_{2-x}Sr_xCuO_4$ Films under Tensile Strain

In this chapter the work on films under tensile strain is discussed. Based on the conclusions from the measurements on $La_{2-x}Sr_xCuO_4$ films under compressive strain, the question arises: What electronic band structure would one expect for the opposite situation, namely $La_{2-x}Sr_xCuO_4$ films under *tensile* strain?

6.1 Expected and Measured Fermi Contours

We were presuming an evolution of the Fermi surface like in figure 6.1(a), where *Fermi contour* changes are shown (see chapter 4.2). In this picture the Fermi contour evolves continuously. In the case of compressive strain the Fermi contour is electron-like.

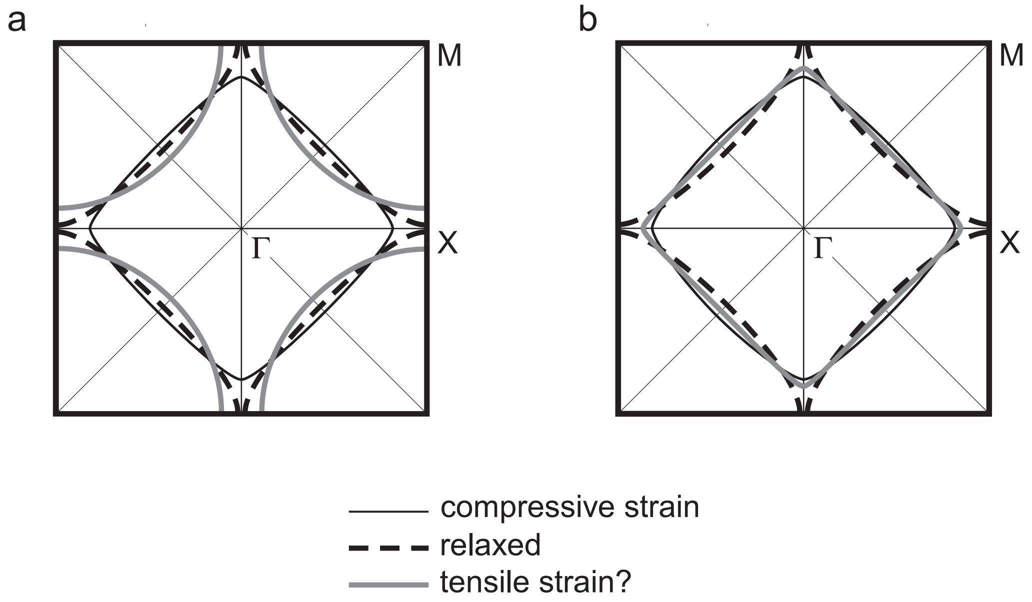

Figure 6.1 (a) and (b): Two presumed Fermi contours for $La_{2-x}Sr_xCuO_4$ under tensile strain

By diminishing the compressive strain, the band crossing along $\Gamma - X$ disappears and for an optimally doped film, the Fermi contour is hole-like. Now the strain is changed and tensile strain is applied. For increasing strain, the Fermi contour approaches the Γ point, whereas the distance between the Fermi contour and the X point increases. From this point of view, the situation with no strain (corresponding to a relaxed film or a bulk sample), is not special. However, there is always some strain present in a film due to the different lattice constants of the CuO_2 planes and the LaO planes [6.1, 6.2].

A second possibility that we took into account is represented in figure 6.1(b). Here the case of no strain can be seen as an equilibrium state. The deviation from this equilibrium would provoke similar changes for compressive and for tensile strain. In both cases the Fermi contour would be electron-like.

As we will show in this chapter, the changes of the Fermi surface for films under tensile strain are again rather drastic and largely unexpected. It was much more difficult to obtain ARPES spectra and moreover to analyze the data. As it turned out the Fermi surface is 3-dimensional, which a priori we did not foresee. So the analysis of the incomplete set of measurements was quite evolved.

With the experience acquired during the ARPES measurements on $La_{2-x}Sr_xCuO_4$ films under in-plane compressive strain, we turned our attention towards the properties of films under tensile strain. Since overdoped films showed the best ARPES signal under compressive strain, we decided initially to continue with overdoped films, in early study of tensile strain by ARPES. Subsequently ARPES measurements were also performed on optimally doped films.

Despite a careful search for optimal growth conditions, the ARPES measurements turned out to be more demanding than for films under compressive strain. A very meticulous optimization of the film growth parameters, as described in chapter 3, was necessary. Several 3-week beamtime periods were needed before a dispersing photoemission signal could be observed. Namely, the noise and the background made it difficult to extract the dispersion.

Ultimately, ARPES measurements have been performed at a photon energy of 60 eV, where the signal was the strongest. For photon energies of 20, 30, 40 and 50 eV no clear coherent signal could be observed. Even for 60 eV, the dispersion could only be discerned in a small binding energy range of 0.25 eV. On compressively strained films the signal was strongest at 60 eV too, whereas we observed the best signal on relaxed films at 30 eV.

The 10 films under tensile strain exhibiting a dispersing signal have a *c*-axis of ~13.10 Å, corresponding to a compression of 1% and to strong in-plane tensile strain. The most successful measurements have been performed on $La_{2-x}Sr_xCuO_4$ films grown on $SrTiO_3$ substrates, but a dispersion could also be observed on films grown on $SrLaGaO_4$ substrates. The two films that are presented and discussed in this chapter are grown on $SrTiO_3$ substrates, one is overdoped (233LO, $x = 0.2$), the other one optimally doped (251L, $x = 0.15$).

For both films the observed Fermi contour does not correspond to the expected, 2-dimensional Fermi surface schematically shown in figures 6.1(a) or 6.1(b). It does not seem to respect the Luttinger rule [6.3] for the nominal hole doping, given by the *Sr* content of the two films. The situation is illustrated in figure 6.2 for the film 233LO. The band filling for the observed Fermi contour would correspond to $x \cong -0.20$, i.e. to electronic doping for both films.

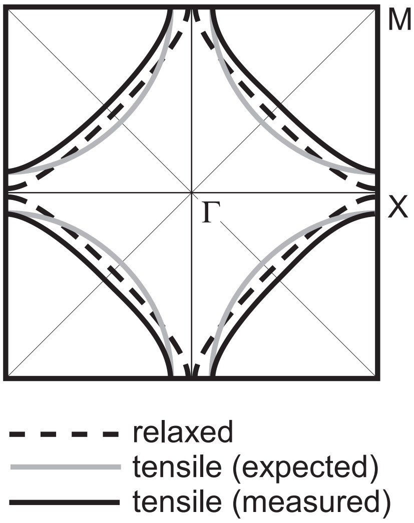

Figure 6.2: The Fermi contour determined from ARPES measurements on the sample 233LO encloses a surface that is larger than expected for an overdoped $La_{1.8}Sr_{0.2}CuO_4$ *film. The Luttinger rule does not seem to be obeyed.*

Attempts to fit the dispersion within the 2-dimensional generic tight binding approach presented in chapter 4 did not lead to success. Even if a misalignment of the analyzer chamber was taken into account, it seems impossible to fit the measured data consistently. The fits were not better when a band filling corresponding to electronic doping was used, as recommended by the observed Fermi crossings (a structural change from the *T* to the *T'* phase of the $La_{2-x}Sr_xCuO_4$ unit cell might be at the origin of such a different band filling).

6.2 Three-Dimensional Dispersion

All these preceding observations were taken as an indication of a 3-dimensional dispersion, as opposed to the 2-dimensional dispersion of films that are relaxed or under compressive strain, as described in the last chapter or for bulk crystals [6.4, 6.5].
The importance of out-of-plane orbitals and 3-dimensional dispersion has been studied by several theorists.

In [6.6] Bansil et al. discuss the possibility of 3-dimensional dispersion in HTSC. Only bulk crystals are considered, whereas the effect of strain, which may enhance or diminish the 3-dimensional character of the dispersion, is not taken into account. Their conclusion is that the effect of 3-dimensional dispersion on ARPES measurements should be detectable with currently available high resolution analyzers. As a particular case in [6.6] $Bi_2Sr_2CaCu_2O_8$ is studied. There, the effect of 3-dimensional dispersion is predicted to be a broadening of the linewidth. For $La_{2-x}Sr_xCuO_4$ and some other materials they expect an even larger effect of 3-dimensional dispersion.

It was K. A. Müller who pointed out to us the paper and consequences of the analysis of D. I. Khomskii and E. I. Neimark [6.7]. The fact that the $Cu3d_{3z^2-r^2}$ level becomes relevant in $La_{2-x}Sr_xCuO_4$ is discussed. As a possible mechanism for this effect they suggest a change of the crystal field splitting due to the Coulomb interaction between the *Cu3d* electrons and the *O2p* holes. The picture presented in figure 1.3 seems to be too simple, since it does not take into account the participation of other copper orbitals.

O. K. Andersen et al. [6.8] identify in their analysis the energy of the out-of-plane orbital as the main material dependent parameter, which controls the intralayer hopping range *r*. They observe that materials with a higher T_C at optimal doping exhibit usually a larger *r* and more localized out-of-plane orbitals. The out-of-plane orbital of such materials, has almost pure *Cu4s* character. As example among single-layer HTSC they cite $HgBa_2CuO_4$ and $Tl_2Ba_2CuO_6$. Materials like $La_{2-x}Sr_xCuO_4$ (with a relatively low T_C at optimal doping) have out-of-plane orbitals with a hybrid character. Besides *Cu4s*, contributions from $Cu3d_{3z^2-r^2}$, apical $O2p_z$ and $La5d_{3z^2-r^2}$ become important too, or even dominant.

A 3-dimensional Fermi surface in HTSC has even been observed by N. E. Hussey et al. [6.9]. They measured polar angular magnetoresistance oscillations (AMRO) in overdoped $Tl_2Ba_2CuO_{6+\delta}$ bulk crystals and found that the Fermi surface has the shape of a warped cylinder (see figure 6.8 where it is compared to the reconstructed Fermi surface of our sample).

The interpretation of a 3-dimensional dispersion is also supported by the selection rules as explained in figure 4.5. In $La_{2-x}Sr_xCuO_4$ films we see a signal also in a direction ($\varphi = 45°$) that is forbidden for a dispersion arising only from the $Cu3d_{x^2-y^2}$ and *O2p* orbitals. If orbitals with other symmetries are also participating in the conduction, this direction is no longer forbidden.

What mechanism could be at the origin of the strong enhancement of 3-dimensional dispersion for films under tensile strain?

Among the cuprates, $La_{2-x}Sr_xCuO_4$ is the one with the shortest apical oxygen distance. Through in-plane tensile strain the copper atom and its apical oxygen are brought closer together, thus increasing the overlap of their orbitals and hence opening a gate for conduction along the third dimension. Locquet et al. performed X-ray diffraction measurements on $La_{2-x}Sr_xCuO_4$ films under tensile strain grown on $SrTiO_3$. Their refinement shows [6.10] that the distance between the copper atom and the apical oxygen is indeed diminished, as expected. In contrast, compressive in-plane strain has the opposite effect, the copper atom and the apical oxygen are elongated (see last chapter) and the observed Fermi surface is 2-dimensional.

When we performed our measurements on films under tensile strain, we did not expect a 3-dimensional dispersion. Thus, we did not concentrate on measurements at different photon energies. The sample lifetime in the analyzer chamber being limited, we tried to do ARPES measurements at as many φ angles as possible.

The measured data set by itself is therefore insufficient for a precise reconstruction of the actual Fermi surface. Nevertheless, it can be used to confirm the 3-dimensional character of the dispersion and to verify if the 3-dimensional generic tight binding approach can be used to fit the observed dispersion. The resulting Fermi surface, although not strictly exact, can serve as a sketch for further ARPES studies, which will provide a much more accurate Fermi surface.

The dispersion of the sample 233OD for the angles φ = 0° (Γ– X), φ = 10° and φ = 45° (Γ– M) is shown in figure 6.3 in the momentum density curve representation. The measured spectra have been normalized.

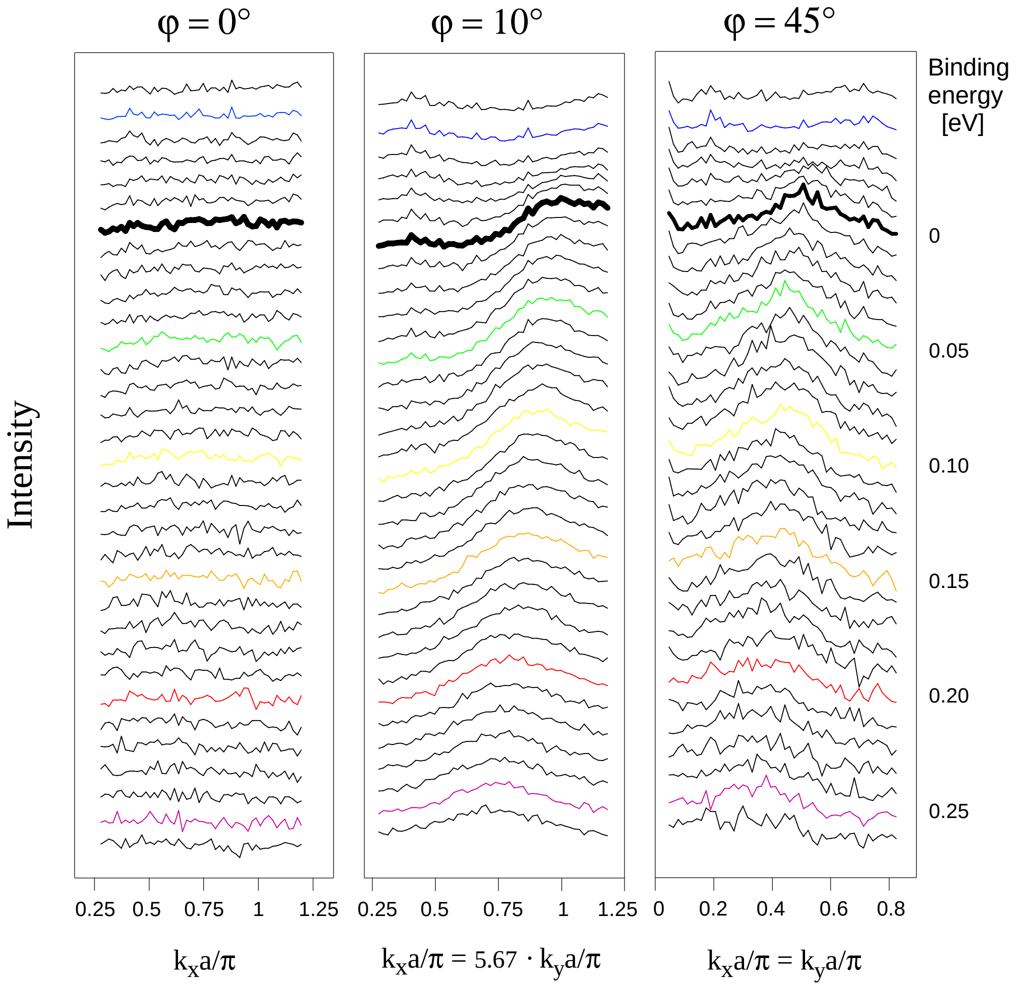

Figure 6.3: Momentum density curves from an ARPES measurement for different φ angles: φ = 0° (Γ–X), φ = 10° and φ = 45° (Γ–M) for an overdoped $La_{1.8}Sr_{0.2}CuO_4$ film under tensile strain (233LO).

For φ = 0° no dispersing signal is detected, whereas for φ = 10° and φ = 45° a peak can be observed that evolves towards the Fermi level and crosses it.

For this particular film, measurements have been performed at φ = 0°, φ = 5°, φ = 10°, φ = 30° and φ = 45°. Except for φ = 0° (no dispersing signal), they are fitted with the generic tight binding approach (figure 6.4).

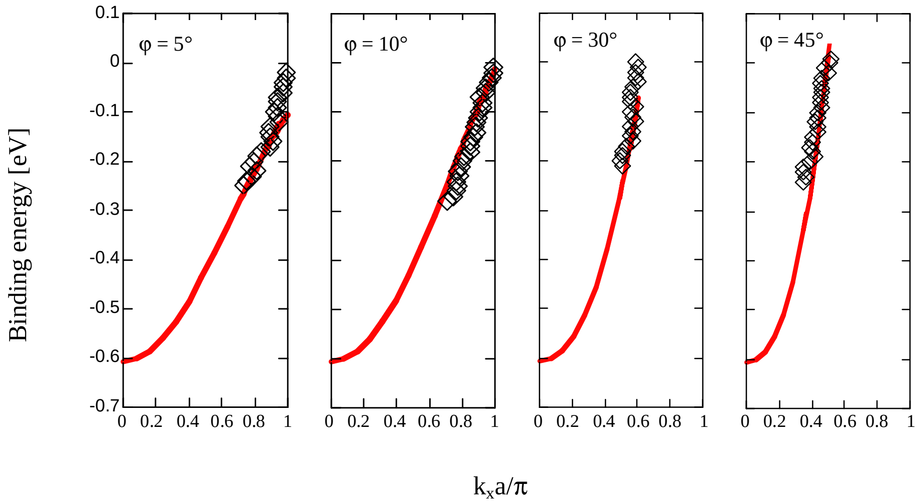

Figure 6.4: ARPES measurements along selected φ angles and fit for an overdoped $La_{1.8}Sr_{0.2}CuO_4$ film under tensile strain (233LO). The dimensions of the squares correspond to the estimated error.

The parameters have been varied to find the best agreement. The overall agreement is acceptable, but there are some deviations between fit and measurement, especially at low φ angles. The 3-dimensional Fermi surface resulting from the best fitting parameters (table 6.1) is shown in figure 6.5, where it is compared to the 2-dimensional Fermi surface of a relaxed $La_{1.8}Sr_{0.2}CuO_4$ film.

Fitting parameter	233 LO (overdoped)	251L (optimally doped)
t	0.25 eV	0.22 eV
r	0.3	0.3
μ	7.71	9.82
ν	0.15	0.15
E_0	0.6 eV	0.62 eV
m*	1.18 m_e	1.23 m_e

Table 6.1: Best fitting parameters determined from the ARPES measurements on the films 233LO and 251L

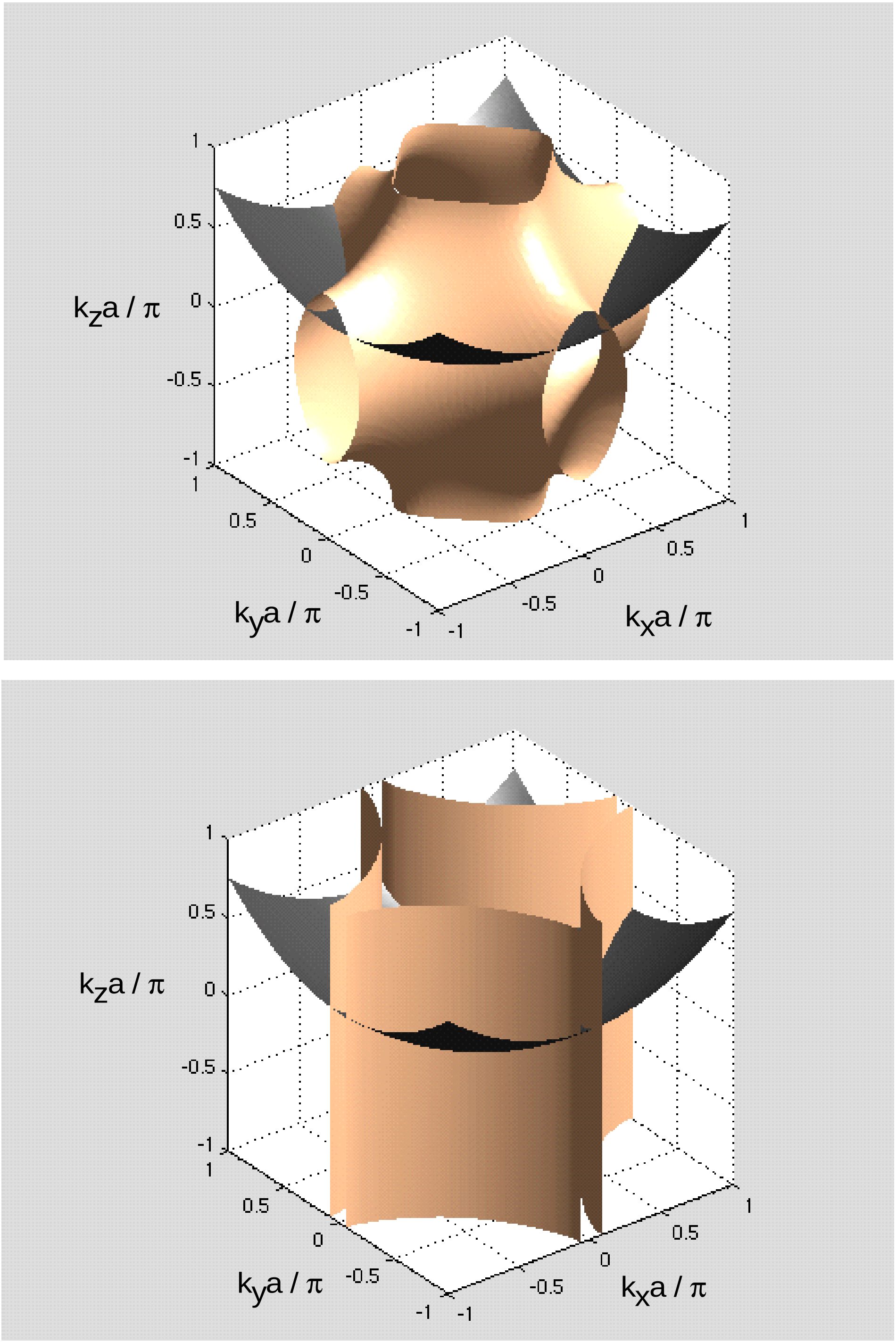

Figure 6.5: Reconstructed 3-dimensional Fermi surface for an overdoped $La_{1.8}Sr_{0.2}CuO_4$ *film under tensile strain (top) and 2-dimensional Fermi surface for a relaxed* $La_{1.8}Sr_{0.2}CuO_4$ *film (bottom). The black surface is the probing sphere for the photon energy* $h\nu = 60$ *eV.*

The dispersion in the third dimension is quite important and changes the Fermi surface significantly. The fitting parameter ν, which controls the dispersion along k_z, is 0.15 ($\nu = 0$ for 2-dimensional dispersion). The modulation of the Fermi surface along k_z leads to tubular connections of adjacent Fermi surfaces at the Brillouin zone boundaries, which are called necks. The Fermi surface of sample 251L is similar (figure 6.6) to the one of 233LO, the same difficulties for the fit are encountered in both cases close to the necks.

The constant photon energy sphere corresponding to the Fermi energy (equation 4.13) cuts the Fermi surface and passes through the center of the in-plane necks, whereas in 233LO the cut is close to the upper limit of the necks. This difference is due to a slightly higher effective mass for the optimally doped film 251L, presumably associated with its weaker metallic screening.

The parameter r characterizing the relative in-plane hopping probabilities evolves only weakly with doping. The ratio r is essentially affected by strain. For films under compressive strain, it drops to 0.036, compared to 0.27 for an overdoped relaxed film (see chapter 5). For the tensile-strained 233LO, r changes only slightly to 0.3, the huge change is on ν. These changes are opposite to what one would expect from the changes in the overlap of the in-plane orbitals.

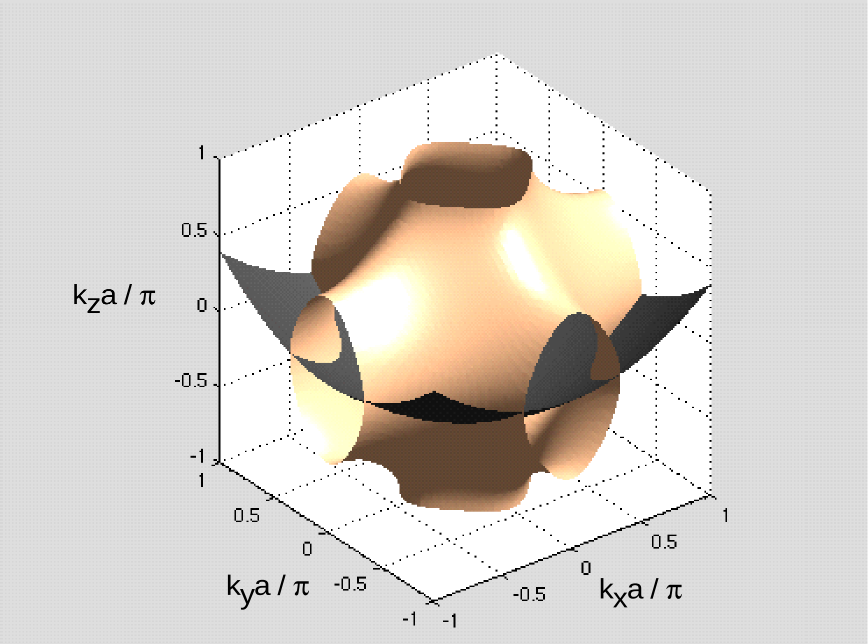

Figure 6.6: Reconstructed 3-dimensional Fermi surface of the optimally doped 251L and the black probing sphere for the photon energy $h\nu = 60$ eV.

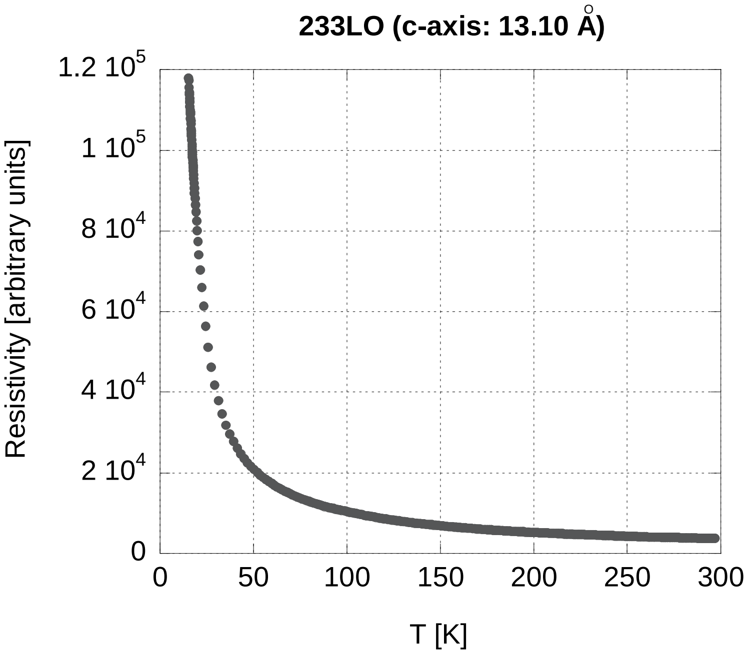

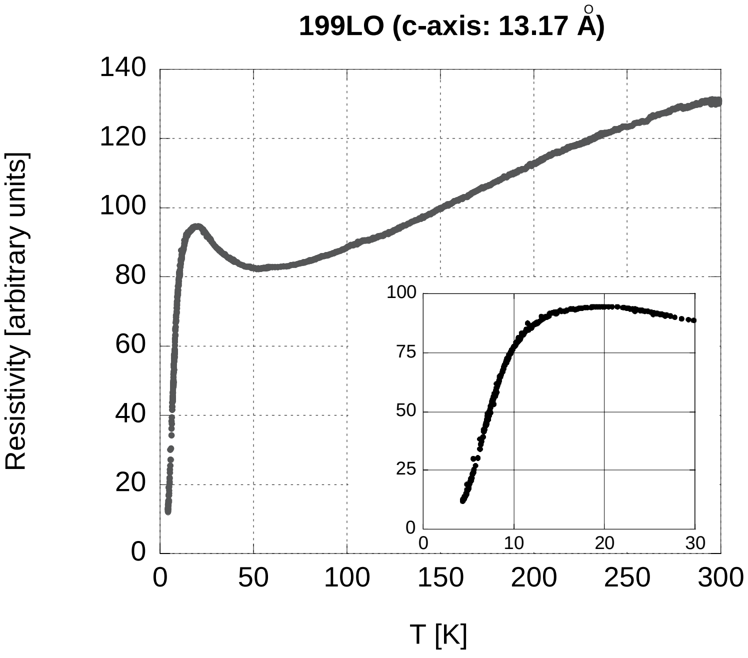

Figure 6.7: Resistivity measurement on the overdoped $La_{1.8}Sr_{0.2}CuO_4$ *films 233LO (under huge tensile strain) and 199LO (under tensile strain)*

Resistivity measurements on 233LO and 251L do not show any sign of superconductivity, on the contrary, the curves show an insulating behavior for these samples (figure 6.7). The tensile strain completely suppressed superconductivity. In an overdoped sample, where the strain is less important, but still considerable (*c*-axis: 13.17 Å), we observe a T_C onset at 18 K (figure 6.7). T_C has been reduced strongly, as compared to relaxed $La_{1.8}Sr_{0.2}CuO_4$.

ARPES measurements on such samples with intermediate strain were not successful, most likely because misfit dislocations due to partial relaxation diminish the coherence necessary for ARPES.

In figure 6.8 the projection of the reconstructed Fermi surface from 233LO and from the $Tl_2Ba_2CuO_{6+\delta}$ crystal of [6.9] are compared. The $Tl_2Ba_2CuO_{6+\delta}$ Fermi surface is a slightly warped cylinder. In our sample, the distortions of the original cylinder are much bigger and show, what a huge influence strain can have on the electronic dispersion. The $Tl_2Ba_2CuO_{6+\delta}$ crystal is still a HTSC with a T_c of 20 K, whereas in our film there is no superconducting transition anymore.

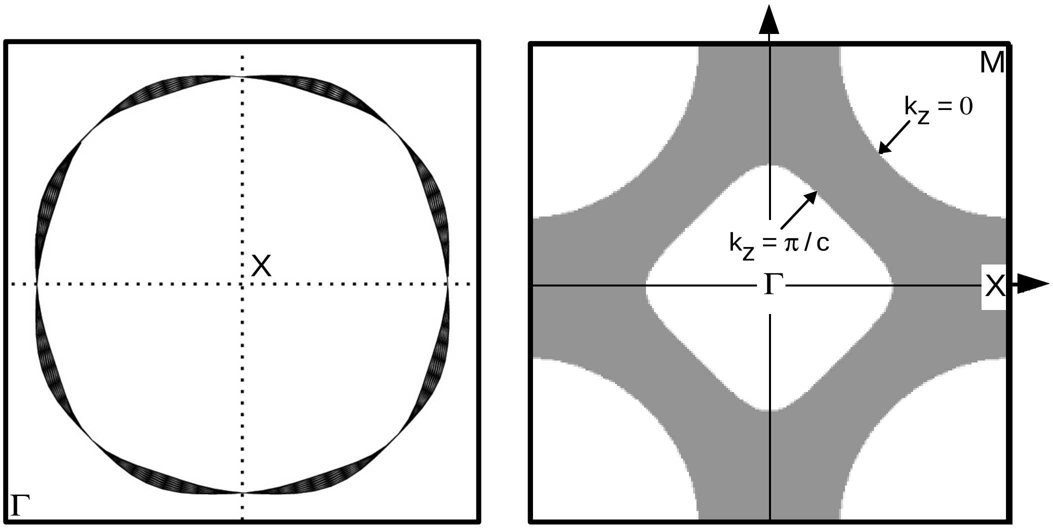

Figure 6.8: Projection of the reconstructed Fermi surface of an overdoped $Tl_2Ba_2CuO_{6+\delta}$ *crystal with AMRO measurements (left, for details see [6.9]) and of our overdoped* $La_{1.8}Sr_{0.2}CuO_4$ *film 233LO with ARPES measurements (right)*

In summary, we note that ARPES on tensile-strained samples is experimentally very demanding, yet we have succeeded to get the first set of data. The analysis of our ARPES measurements shows that the dispersion observed on $La_{2-x}Sr_xCuO_4$ films under tensile strain can be accounted for assuming that the dispersion is 3-dimensional. With the generic tight binding approach it is possible to fit the data, although the agreement is not quite satisfactory near the necks in the Fermi surface.

Further ARPES measurements at different photon energies are required, so that the detailed Fermi surface can be mapped, as illustrated in figure 6.9.

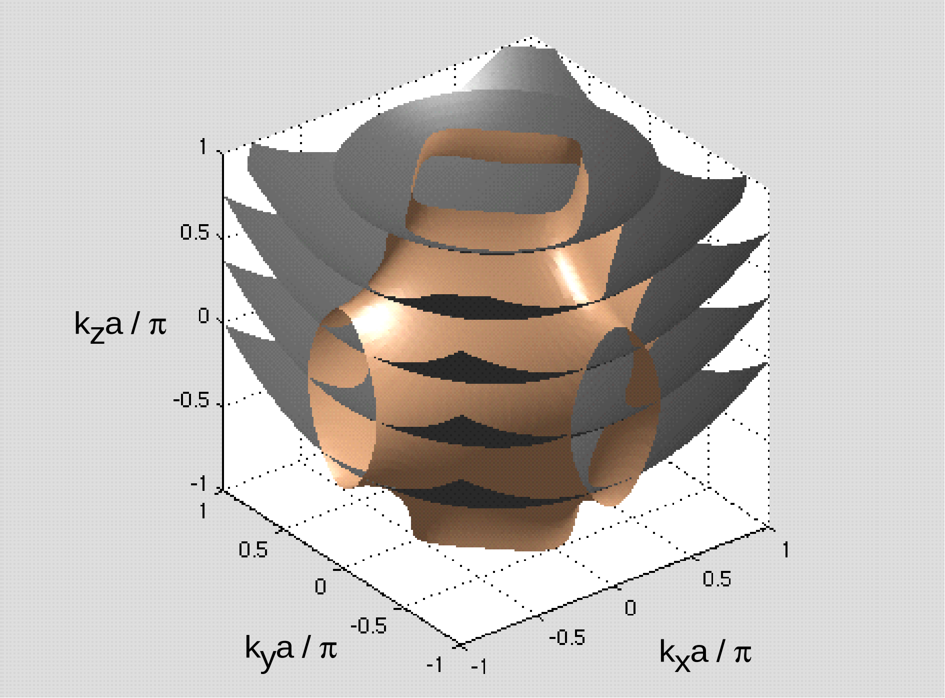

Figure 6.9: ARPES measurements at different photon energies allow mapping the whole Fermi surface. The probing spheres have photon energies of 65 eV, 62.5 eV, 60 eV, 57.5 eV and 55 eV.

However, the main features of the emerging physical pictures can be outlined: To account for the changes in electronic structure and superconductivity, the out-of-plane states should be clearly taken into consideration, as well as some subtle changes in associated lattice parameters.

Chapter 7: Conclusions and Outlook

ARPES measurements on HTSC thin films show surprising effects of strain on the electronic properties. These measurements were made possible through the development of a unique experimental chain at the Synchrotron Radiation Center in Wisconsin, allowing us to control every step from the film growth by pulsed laser deposition, over the sample transfer into the analyzer chamber in high purity oxygen, to the ARPES measurements with synchrotron radiation. After an optimization process, we are able to grow with this system thin films of a thickness varying from about one unit cell to several hundred Angstroms, and with a surface quality suitable for ARPES experiments. The combination of PLD and ARPES allows us to study materials, that cannot be cleaved, or effects like strain, that are inherent to thin films and cannot be observed in bulk samples.
With our measurements, we have launched a new experimental approach, which is by now used by several groups that combine either PLD or MBE and ARPES for measurements on as-grown samples.

Initial ARPES measurements on optimally doped $La_{2-x}Sr_xCuO_4$ films revealed a huge influence of compressive strain on the electronic dispersion. It enhances the dispersion and the Fermi surface is electronlike (centered around Γ), in contrast to unstrained bulk crystals, where a holelike (centered around M) Fermi surface has been deduced from ARPES measurements [7.1, 7.2]. The density of states near the Fermi level is therefore diminished in films under compressive strain, as compared to the bulk samples. According to many mean field models, such a decrease of the density of states does not favor an increase of T_C. However, we observed an increase of T_C for all our films under compressive strain.
On overdoped films we were able to confirm this behavior under strain. Moreover, we have established the equivalence of ARPES measurements on uncleaved relaxed films and scraped bulk crystals; namely the measurements on our relaxed films give same results as the measurements on scraped bulk crystals performed by Ino, Fujimori, Shen and Uchida et al. [7.2], hence ruling out an explanation through finite size effects other than strain.
As mentioned in chapter 5, complementary studies on our films under compressive strain by EXAFS, reflection and Raman spectroscopy are still in progress, yet all preliminary results are in accordance with discussions given in this thesis.

Our recent ARPES measurements on $La_{2-x}Sr_xCuO_4$ films under huge in-plane tensile strain (compressing the c-axis by 1%) indicate a dispersion that is no longer 2-dimensional, as it is the case for films under compressive strain. Under tensile strain, the dispersion has also an important component in the direction perpendicular to the CuO_2 plane. On the basis of a restricted set of measured data and with a generic tight binding approach we have reconstructed the 3-dimensional Fermi surface.

Our obtained Fermi surface still has to be thoroughly verified in further experiments. It helps us to plan the next ARPES experiments, especially for the determination of the photon energies that should be used for a more complete mapping of the Fermi surface.

Our generic tight binding approach and the three-step model are employed with several underlying approximations. They proved to be very useful for the analysis of our first data on films under tensile strain. However, for an advanced analysis of a more complete set of data they should be refined.

Resistivity measurements on the films under tensile strain on which ARPES measurements had been performed do not exhibit superconductivity. Films, in which the tensile strain is weaker, still show a transition to the superconducting state at a T_C that is lower compared to relaxed films.

Our analysis shows that tensile strain brings the apical oxygen closer to the Cu atom and the overlap of their orbitals is increased, enhancing 3-dimensionality. The increase of the 3-dimensional character of the dispersion coincides with the disappearance of superconductivity.

Considering the strong influence of strain, both tensile and compressive, on T_C, the phase diagram for $La_{2-x}Sr_xCuO_4$ from figure 1.4 has to be extended by a third axis for strain. The resulting phase diagram probably resembles to the one shown in figure 7.1.

The purpose of this diagram is illustrative only, as further studies are required to confirm all implications and trends. So far, measurements have been performed only at few doping values and do not allow tracing the whole phase diagram. We concentrated on the transition to the superconducting state, without examining the effect of strain on the transition to the pseudogap state or on the transition from an antiferromagnetic insulator to a metal. How these transitions are affected by strain and many other questions related to strain can be addressed, now that the growth of $La_{2-x}Sr_xCuO_4$ films under compressive and tensile strain has been optimized and that systematic ARPES measurements are possible. Undoubtedly, this is a very promising experimental approach to eventually understand the mechanism of high-T_C superconductivity.

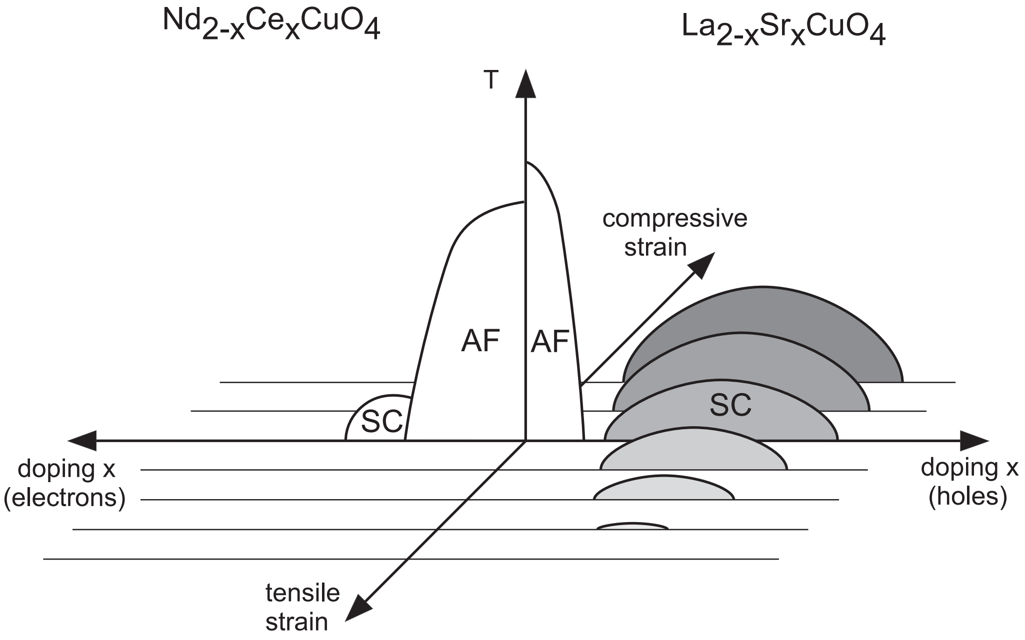

Figure 7.1: Phase diagram of $La_{2-x}Sr_xCuO_4$ (and its electron-doped counterpart $Nd_{2-x}Ce_xCuO_4$) taking into consideration compressive and tensile strain for the superconducting phase (SC). AF is the insulating antiferromagnetic phase. Note that for electron-doped compounds there are no strain data.

References

Chapter 1

[1.1] I. Mrkonjic and S. Barisic, *Comment on ‘‘Strain and High Temperature Superconductivity: Unexpected Results from Direct Electronic Structure Measurements in Thin Films’’*, Phys. Rev. Lett. **92**, 129701 (2004);
Abrecht *et al.*, *Reply*, Phys. Rev. Lett. **92**, 129702 (2004)

[1.2] H. Kamerlingh-Onnes, *On the change of the electrical resistance of pure metals at very low temperatures,* Leiden Commun. **120b**, **122b**, **124c** (1911)

[1.3] R. de Bruyn Ouboter, *SUPERCONDUCTIVITY: DISCOVERIES DURING THE EARLY YEARS OF LOW TEMPERATURE RESEARCH AT LEIDEN 1908 – 1914,* IEEE Transactions on Magnetics **23**, 2 (1987)

[1.4] W. Meissner and R. Oschenfeld, *Ein neuer Effekt bei Eintritt der Supraleitfähigkeit*, Naturwiss. **21**, 787 (1933)

[1.5] F. London and H. London, *The Electromagnetic Equations of the Supraconductor,* Proc. R. Soc. London, **A 149**, 71 (1935)

[1.6] V. L. Ginzburg and L. D. Landau, *ON THE THEORY OF SUPERCONDUCTIVITY*, Zh. Eksp. Teor. Fiz., **20**, 1064 (1950)

[1.7] J. Bardeen, L. N. Cooper, and J. R. Schrieffer, *Theory of Superconductivity,* Phys. Rev. **108**, 5, 1175 (1957)

[1.8] B. D. Josephson, *POSSIBLE NEW EFFECTS IN SUPERCONDUCTIVE TUNNELLING*, Phys. Lett. **1**, 251 (1962)

[1.9] J. G. Bednorz and K. A. Müller, *Possible High* T_C *Superconductivity in the Ba-La-Cu-O System*, Z. Phys. B **64**, 189 (1986)

[1.10] A. Schilling *et al.*, *Superconductivity above 130 K in the Hg−Ba−Ca−Cu−O system*, Nature **363**, 56 (1993)

[1.11] L. Gao *et al.*, *Superconductivity up to 164K in* $HgBa_2Ca_{m-1}Cu_mO_{2m+2+\delta}$ *(m = 1, 2, and 3) under quasihydrostatic pressures*, Phys. Rev. B **50**, 4260 (1994)

[1.12] J. Nagamatsu *et al.*, *Superconductivity at 39K in magnesium diboride,* Nature **410**, 63 (2001)

[1.13] P. Brusov, *Mechanisms of High Temperature Superconductivity*, Rostov State University Publishing (1999)

[1.14] A. Bussmann-Holder and H. Keller, *Polaron formation as origin of unconventional isotope effects in cuprate superconductors*, Eur. Phys. J. B **44**, 487 (2005)

[1.15] J. Hubbard, *Electron correlations in narrow energy bands*, Proc. Roy. Soc. **276**, 1365, 238 (1963)

[1.16] V. J. Emery, *Theory of High-T_C Superconductivity in Oxides*, Phys. Rev. Lett. **58**, 2794 (1987)

[1.17] J. C. Phillips, *Topological Theory of Electron-Phonon Interactions in High Temperature Superconductors,* www.arxiv.org/ftp/cond-mat/papers/0408/0408040.pdf (2003)

[1.18] D. Ariosa, H. Beck, *A POSSIBLE PAIRING MECHANISM FOR HTSC: TWO-DIMENSIONAL CONFINEMENT AND COULOMB OVER-SCREENING,* IJMP B **13**, 3472 (1999)

[1.19] C. P. Poole *et al.*, *Superconductivity,* Academic Press (1995) and references therein

[1.20] G. Margaritondo, *Introduction to Synchrotron Radiation,* Oxford University Press (1988)

[1.21] J. C. Campuzano *et al.*, *Photoemission in the High T_C Superconductors*, in "The Physics of Superconductors" edited by K.-H. Bennemann and J. B. Ketterson, Springer (2003)

[1.22] P. R. Willmott *et al., PULSED LASER DEPOSITION AT THE SLS,* http://sls.web.psi.ch/view.php/science/docs/annual/Willmott03.pdf

[1.23] H. Yamamoto *et al., In situ angle-resolved photoemission study of MBE-grown* $(La,Ce)_2CuO_4$ *thin films*, Physica C **412-414**, 134 (2004)

[1.24] M. Cyrot and D. Pavuna, *INTRODUCTION TO SUPERCONDUCTIVITY AND HIGH-T_C MATERIALS,* World Scientific (1992)

[1.25] M. Imada *et al.*, *Metal-insulator transitions,* Rev. Mod. Phys. **70**, 1039 (1998)

[1.26] M. Abrecht, *PHOTOEMISSION STUDIES OF THIN FILMS GROWN BY PULSED LASER DEPOSITION; EPITAXIAL STRAIN EFFECTS ON THE ELECTRONIC STRUCTURE OF HIGH TEMPERATURE SUPERCONDUCTORS*, PhD thesis, EPFL (2003)

[1.27] I. Vobornik, *INVESTIGATION OF THE ELECTRONIC PROPERTIES AND CORRELATION EFFECTS IN THE CUPRATES AND IN RELATED TRANSITION METAL OXIDES*, PhD thesis, EPFL (1999)

[1.28] P. G. Radaelli *et al.*, *Structural and superconducting properties of* $La_{2-x}Sr_xCuO_4$ *as a function of Sr content*, Phys. Rev. B **49**, 6, 4163 (1994)

[1.29] H. Sato and M. Naito, *Increase in the superconducting transition temperature by anisotropic strain effect in (001)* $La_{1.85}Sr_{0.15}CuO_4$ *thin films on* $LaSrAlO_4$ *substrates*, Physica C **274**, 221 (1997)

[1.30] J. P. Locquet *et al.*, *Doubling the critical temperature of* $La_{1.9}Sr_{0.1}CuO_4$ *using epitaxial strain*, Nature **394**, 453 (1998);

J. P. Locquet *et al.*, *Changes of* T_c *under epitaxial strain: Implications for the mechanism of superconductivity*, Proc. SPIE Int. Soc. Opt. Eng. **3481**, 248 (1998)

[1.31] I. Bozovic *et al.*, *Epitaxial Strain and Superconductivity in* $La_{2-x}Sr_xCuO_4$ *Thin Films*, Phys. Rev. Lett. **89**, 107001 (2002)

[1.32] D. Ariosa *et al.*, *Structural Properties of Strained* $YBa_2Cu_3O_{6+x}$ *Superconducting Films Grown by Pulsed Laser Deposition*, Proc. SPIE Int. Soc. Opt. Eng. **4058**, 129 (2000)

[1.33] A. Gauzzi, *DISORDER AND FLUCTUATIONS IN SUPERCONDUCTING* $YBa_2Cu_3O_{6.9}$ *FILMS*, PhD thesis, EPFL (1993)

Chapter 2

[2.1] D. B. Chrisey and G. K. Hubler, *Pulsed Laser Deposition of Thin Films*, John Wiley & Sons (1994) and references therein

[2.2] A. Einstein, *Zur Quantentheorie der Strahlung*, Physik. Zeitschr. **XVIII**, 121 (1917)

[2.3] J. P. Gordon *et al.*, *Molecular Microwave Oscillator and New Hyperfine Structure in the Microwave Spectrum of* NH_3, Phys. Rev. **95**, 282 (1954)

[2.4] T. H. Maiman, *Stimulated Optical Radiation in Ruby*, Nature **187**, No. 4736, pp. 493 (1960)

[2.5] H. M. Smith and A. F. Turner, *Vacuum Deposited Thin Films Using a Ruby Laser*, Applied Optics **4**, 1 (1965)

[2.6] D. Dijkkamp *et al.*, *Preparation of Y-Ba-Cu oxide superconductor thin films using pulsed laser evaporation from high* T_C *bulk material*, Appl. Phys. Lett. **51** (8), 619 (1987)

[2.7] Q. X. Jia *et al.*, *High-temperature superconducting thick films with enhanced supercurrent carrying capability*, Appl. Phys. Lett. **80** (9), 1601 (2002)

[2.8] Y. Zhang *et al.*, *Single-wall carbon nanotubes synthesized by laser ablation in a nitrogen atmosphere*, Appl. Phys. Lett. **73** (26), 3827 (1998)

[2.9] T. J. Goodwin *et al.*, *Synthesis of gallium nitride quantum dots through reactive laser ablation*, Appl. Phys. Lett. **70** (23), 3122 (1997)

[2.10] M. Abrecht *et al.*, *Structural phase transition in early growth of $Bi_2Sr_2CaCu_2O_{8+x}$ films on STO substrates*, Journal of Applied Physics **91** (3), 1187-1190 (2002)

[2.11] J. A. Thornton, *HIGH RATE THICK FILM GROWTH*, Ann. Rev. Mater. Sci. **7**, 239 (1977)

[2.12] R. K. Singh and J. Narayan, *Pulsed-laser evaporation technique for deposition of thin films: Physics and theoretical model*, Phys. Rev. B **41** (13), 8843 (1990)

[2.13] D. Ariosa *et al.*, *Structural Properties of Strained $YBa_2Cu_3O_{6+x}$ Superconducting Films Grown by Pulsed Laser Deposition*, Proc. SPIE Int. Soc. Opt. Eng. **4058**, 129 (2000)

Chapter 3

[3.1] M. Abrecht *et al.*, *Surface Optimization of R-$Ba_2Cu_3O_{7-\delta}$ (R=Y, Nd) Epitaxial High-T_C films for In-situ Photoemission Studies*, Surface Review and Letters **7**, 4, 495 (2000)

[3.2] M. Abrecht *et al.*, *On the detection of the Fermi edge in in-situ grown thin films of high-T_C oxide*s, Physica C **364-365**, 538 (2001)

[3.3] M. Abrecht, *PHOTOEMISSION STUDIES OF THIN FILMS GROWN BY PULSED LASER DEPOSITION; EPITAXIAL STRAIN EFFECTS ON THE ELECTRONIC STRUCTURE OF HIGH TEMPERATURE SUPERCONDUCTORS*, PhD thesis, EPFL (2003)

[3.4] A. De-Lozanne, *Scanning probe microscopy of high-temperature superconductors*, Supercond. Sci. Technol. **12**, R43 (1999)

[3.5] A. Guinier, *THEORIE ET TECHNIQUE DE LA RADIOCRISTALLOGRAPHIE*, Dunod (1956)

[3.6] D. Schwarzenbach, *Cristallographie*, Presses Polytechniques et Universitaires Romandes (1993)

[3.7] P. G. Radaelli *et al.*, *Structural and superconducting properties of* $La_{2-x}Sr_xCuO_4$ *as a function of Sr content*, Phys. Rev. B **49**, 6, 4163 (1994)

[3.8] I. Bozovic *et al.*, *Epitaxial Strain and Superconductivity in* $La_{2-x}Sr_xCuO_4$ *Thin Films*, Phys. Rev. Lett. **89**, 107001 (2002)

Chapter 4

[4.1] S. Mitrovic et al., *Experimental Electronic Structure and Interband Nesting in BaVS3*, http://xxx.lanl.gov/abs/cond-mat/0502144

[4.2] H. Hertz, *Ueber einen Einfluss des ultravioletten Lichtes auf die elektrische Entladung*, Ann. Physik **31**, 983 (1887)

[4.3] G. Margaritondo, *Introduction to Synchrotron Radiation*, Oxford University Press (1988)

[4.4] S. Hüfner, *Photoelectron Spectroscopy: Principles and Applications*, Springer-Verlag (2003) and references therein

[4.5] D. W. Lynch and C. G. Olson, *Photoemission Studies of High Temperature Superconductors*, Cambridge University Press, New York (1999)

[4.6] A. Damascelli *et al.*, *Angle-resolved photoemission spectroscopy of the cuprate superconductors*, Reviews of Modern Physics **75**, 473, (2003)

[4.7] J. C. Campuzano *et al.*, *Photoemission in the High* T_C *Superconductors*, in "The Physics of Superconductors" edited by K.-H. Bennemann and J. B. Ketterson, Springer (2003)

[4.8] C. N. Berglund, W.E. Spicer, *Photoemission Studies of Copper and Silver: Theory*, Phys. Rev. A **136**, 1030 (1964);

C. N. Berglund, W.E. Spicer, *Photoemission Studies of Copper and Silver: Experiment*, Phys. Rev. A **136**, 1044 (1964)

[4.9] M. P. Seah, W. A. Dench, *Quantitative Electron Spectroscopy of Surfaces: A Standard Data Base for Electron Inelastic Mean Free Paths in Solids*, Surface and Interface Analysis **1**, no.1, 1979

[4.10] J. Mesot *et al.*, *Determination of the Fermi surface in high-* T_C *superconductors by angle-resolved photoemission spectroscopy*, Phys. Rev. B **63**, 224516 (2001)

[4.11] J. M. Luttinger, *Fermi Surface and Some Simple Equilibrium Properties of a System of Interacting Fermions*, Phys. Rev. **119**, no. 4 (1960)

Chapter 5

[5.1] M. Abrecht *et al.*, *Strain and High Temperature Superconductivity: Unexpected Results from Direct Electronic Structure Measurements in Thin Films*, Phys. Rev. Lett. **91**, 057002 (2003)

[5.2] M. Abrecht, *PHOTOEMISSION STUDIES OF THIN FILMS GROWN BY PULSED LASER DEPOSITION; EPITAXIAL STRAIN EFFECTS ON THE ELECTRONIC STRUCTURE OF HIGH TEMPERATURE SUPERCONDUCTORS*, PhD thesis, EPFL (2003)

[5.3] H. Sato and M. Naito, *Increase in the superconducting transition temperature by anisotropic strain effect in (001)* $La_{1.85}Sr_{0.15}CuO_4$ *thin films on* $LaSrAlO_4$ *substrates*, Physica C **274**, 221 (1997)

[5.4] J. P. Locquet *et al.*, *Doubling the critical temperature of* $La_{1.9}Sr_{0.1}CuO_4$ *using epitaxial strain*, Nature **394**, 453 (1998);

J. P. Locquet *et al.*, *Changes of* T_c *under epitaxial strain: Implications for the mechanism of superconductivity*, Proc. SPIE Int. Soc. Opt. Eng. **3481**, 248 (1998)

[5.5] E. Pavarini *et al.*, *Band-Structure Trend in Hole-Doped Cuprates and Correlation with* T_{Cmax}, Phys. Rev. Lett. **87**, 047003 (2001)

[5.6] G. G. N. Angilella *et al.*, *Effect of strain-induced electronic topological transitions on the superconducting properties of* $La_{2-x}Sr_xCuO_4$ *thin films,* Eur. Phys. J. B **26**, 67 (2002)

[5.7] E. S. Caixeiro and E. V. L. de Mello, Physica C **353**, *Phase diagram and dependence of the critical temperature* T_c *on the pressure for* $Tl_{0.5}Pb_{0.5}Sr_2Ca_{1-x}Y_xCu_2O_7$, 103 (2001)

[5.8] X. J. Chen *et al.*, *Anisotropy of the superconducting transition temperature under uniaxial pressure*, Phys. Rev. B **64**, 212501 (2001)

[5.9] C.W. Chu *et al.*, *Superconductivity above 150 K in* $HgBa_2Ca_2Cu_3O_{8+\delta}$ *at high pressures*, Nature **365**, 323 (1993)

[5.10] K. A. Müller, *On the macroscopic s- and d-wave symmetry in cuprate superconductors*, Philos. Mag. Lett. **82**, 279 (2002); K. A. Müller, *Where Are We in HTSC?*, J. Supercond. **13**, 863 (2000)

[5.11] J. Orenstein and A. J. Millis, *Advances in the Physics of High-Temperature Superconductivity*, Science **288**, 468 (2000) and the references therein

[5.12] D. W. Lynch and C. G. Olson, *Photoemission Studies of High Temperature Superconductors*, Cambridge University Press, New York (1999)

[5.13] J. C. Campuzano *et al.*, *Electronic Spectra and Their Relation to the* (π, π) *Collective Mode in High-*T_C *Superconductors*, Phys. Rev. Lett. **83**, 3709 (1999)

[5.14] D. Ariosa *et al.*, *Structural Properties of Strained* $YBa_2Cu_3O_{6+x}$ *Superconducting Films Grown by Pulsed Laser Deposition*, Proc. SPIE Int. Soc. Opt. Eng. **4058**, 129 (2000)

[5.15] M. Abrecht *et al.*, *Surface Optimization of* $R\text{-}Ba_2Cu_3O_{7-\delta}$ *(R=Y, Nd) Epitaxial High-*T_C *films for In-situ Photoemission Studies*, Surface Review and Letters **7**, 4, 495 (2000)

[5.16] M. R. Norman *et al.*, *Momentum distribution curves in the superconducting state,* Phys. Rev. B **64**, 184508 (2001)

[5.17] A. Ino *et al.*, *Doping-dependent evolution of the electronic structure of* $La_{2-x}Sr_xCuO_4$ *in the superconducting and metallic phases*, Phys. Rev. B **65**, 094504 (2002)

[5.18] A. A. Abrikosov, *Theory of high-*T_C *superconductivity in layered cuprates*, Proc. SPIE Int. Soc. Opt. Eng. **4811**, 1 (2002);

[5.19] J. Bok *et al.* (editors), *The Gap Symmetry and Fluctuations in High-Tc Superconductors*, NATO ASI Series: B **371**, Plenum Press (1998)

[5.20] R. Abd-Shukor, *Acoustic Debye temperature and the role of phonons in cuprates and related superconductors*, Supercond. Sci. Technol. **15**, 435 (2002)

[5.21] I. Mrkonjic and S. Barisic, *Comment on ''Strain and High Temperature Superconductivity: Unexpected Results from Direct Electronic Structure Measurements in Thin Films''*, Phys. Rev. Lett. **92**, 129701 (2004);
Abrecht *et al.*, *Reply*, Phys. Rev. Lett. **92**, 129702 (2004)

[5.22] I. Mrkonjic and S. Barisic, *The Luttinger sum rule in the slave-particle theories,* Eur. Phys. J. B **34**, 441 (2003)

[5.23] P. Brusov, *Mechanisms of High Temperature Superconductivity*, Rostov State University Publishing (1999)

[5.24] I. Bozovic *et al.*, *Epitaxial Strain and Superconductivity in* $La_{2-x}Sr_xCuO_4$ *Thin Films*, Phys. Rev. Lett. **89**, 107001 (2002)

[5.25] P. G. Radaelli *et al.*, *Structural and superconducting properties of* $La_{2-x}Sr_xCuO_4$ *as a function of Sr content*, Phys. Rev. B **49**, 6, 4163 (1994)

[5.26] H. Oyanagi and A. Bianconi (editors), *Physics in Local Lattice Distortions: Fundamentals and Novel Concepts*, AIP Conference Proceedings **554** (2001)

[5.27] K. A. Müller and A. Bussmann-Holder (Editors), *Superconductivity in Complex Systems*, Sructure and Bonding **114**, Springer (2005)

[5.28] A. Bussmann-Holder, *Heterogeneity: the essential ingredient to high T_C superconductivity,* Proc. SPIE Int. Soc. Opt. Eng. **5932**, 33 (2005)

Chapter 6

[6.1] Naito *et al.*, *Phase control in La-214 epitaxial thin films*, Proc. SPIE **4811**, 140 (2002)

[6.2] P. G. Radaelli *et al.*, *Structural and superconducting properties of $La_{2-x}Sr_xCuO_4$ as a function of Sr content*, Phys. Rev. B **49**, 6, 4163 (1994)

[6.3] J. M. Luttinger, *Fermi Surface and Some Simple Equilibrium Properties of a System of Interacting Fermions*, Phys. Rev. **119**, no. 4 (1960)

[6.4] A. Ino *et al.*, *Doping-dependent evolution of the electronic structure of $La_{2-x}Sr_xCuO_4$ in the superconducting and metallic phases*, Phys. Rev. B **65**, 094504 (2002)

[6.5] X. J. Zhou *et al.*, *Dichotomy between Nodal and Antinodal Quasiparticles in Underdoped $La_{2-x}Sr_xCuO_4$ Superconductors*, Phys. Rev. Lett. **92**, 187001 (2004)

[6.6] A. Bansil *et al.*, *Influence of the third dimension of quasi-two-dimensional cuprate superconductors on angle-resolved photoemission spectra*, Phys. Rev. B **71**, 012503 (2005)

[6.7] D. I. Khomskii, E. I. Neimark, *Orbital structure of copper in high temperature superconductors*, Physica C **173**, 342 (1991)

[6.8] E. Pavarini *et al.*, *Band-Structure Trend in Hole-Doped Cuprates and Correlation with T_{Cmax}*, Phys. Rev. Lett. **87**, 047003 (2001)

[6.9] N. E. Hussey *et al.*, *A coherent three-dimensional Fermi surface in a high-transition temperature superconductor*, Nature **425**, 814 (2003)

[6.10] J. P. Locquet *et al.*, *Changes of T_C under epitaxial strain: Implications for the mechanism of superconductivity*, Proc. SPIE Int. Soc. Opt. Eng. **3481**, 248 (1998)

Chapter 7

[7.1] M. Abrecht *et al.*, *Strain and High Temperature Superconductivity: Unexpected Results from Direct Electronic Structure Measurements in Thin Films*, Phys. Rev. Lett. **91**, 057002 (2003)

[7.2] A. Ino *et al.*, *Doping-dependent evolution of the electronic structure of* $La_{2-x}Sr_xCuO_4$ *in the superconducting and metallic phases*, Phys. Rev. B **65**, 094504 (2002)

Acknowledgements

I am most grateful to my thesis advisor Prof. Davor Pavuna for offering me the possibility to participate in this great project, for sending me to about a dozen beamtimes in Madison and to many other beautiful places for summer schools and conferences. I enjoyed much independence and responsibility, when working at the SRC, but at the same time Davor's support was always available. His inexhaustible enthusiasm makes it a pleasure to work with him.

I would like to express my gratitude to Dr. Daniel Ariosa, for introducing me to the secrets of X-ray diffraction and for discussing, always with a lot of humor, the questions that arose to me about superconductivity, photoemission or any other field of physics. No matter how puzzling X-ray or ARPES data are, he develops immediately a model explaining the measurements.

Many thanks to Dr. Mike Abrecht, who introduced me to PLD, the SRC, Culvers, Prime Quarter and to life in Madison. I will never forget all the great beamtimes that we spent together.

Grazie mille to Claudia Cancellieri, I enjoyed to work with her and to see how fast she built and brought to operation the PLD system, which we have designed at the EPFL.

I owe special thanks to Prof. Giorgio Margaritondo for accepting me in his group and for his continuous support.

Thanks a lot to all my friends and colleagues at and around the EPFL: Dr. Dušan Vobornik, Dr. Slobodan Mitrović, Dr. Amela Grošo, Marco Papagno, Pierre-André Baudat, Christian Blumer, Yvonne Stalder, Dr. Bernd Braunecker, Dr. Richard Bossart and many more.

It was a pleasure to work at the SRC and I appreciated the support from the staff and the users. In particular I would like to thank Prof. Gelsomina Puppa De Stasio, Dr. Bradley Frazer, Troy Humphrey and Prof. Marshall Onellion. Especially I would like to thank Dan Wallace for all his help with the PLD, for taking me on canoe trips and for making a prairie fireman out of me.

During this thesis I got a lot of encouragement and support from my family, I will always be thankful to my parents and to my brothers Pascal and Dimitri.
I can never thank enough my wife Issa for her love and her patience during all these years.

Curriculum Vitae

Personal information and present address

Dominique Cloëtta
EPFL SB-IPMC-LPRX
PH D3 314, Station 3
1015 Lausanne, Switzerland

+41 21 6935159
dominique.cloetta@a3.epfl.ch

Date of birth: 15 July 1974
Nationality: Swiss

Education and Professional Experience

2001- 2005	**PhD student and teaching assistant at the Institute of Physics of Complex Matter at the Ecole Polytechnique Fédérale de Lausanne (EPFL).** Research on thin films of superconducting materials. Production of these films by pulsed laser deposition with following analysis by photoemission experiments at synchrotrons in Switzerland (SLS at Villigen) and in the USA (SRC at Madison, in collaboration with the University of Wisconsin).
November 1997 to February 1998	Construction of the electronics and programming (in LabView) to read the images of a low power digital camera, followed by the characterization of its opto-electronic properties at the **Centre Suisse d’Electronique et de Microtechnique** (CSEM).
1994-1997 and 1998- 2001	**Studies of physics at EPFL** with orientation on semiconductors, diploma work on pulsed lasers.

Languages

German	mother tongue
French	fluent
English	fluent
Spanish	conversational

Publications

M. Abrecht, D. Ariosa, D. Cloetta, G. Margaritondo, D. Pavuna, *Electronic Properties of High Temperature Superconducting Thin Films Grown by Pulsed Laser Deposition*, Proc. SPIE Int. Soc. Opt. Eng. **4811**, 102 (2002)

D. Pavuna, M. Abrecht, D. Cloëtta, X.X. Xi, G. Margaritondo, D. Ariosa, *Systematic studies of (magneto)transport, structural and electronic properties of ultra-thin films of high-*T_C *cuprates and related layered oxides*, Current Applied Physics **2**, 345 (2002)

M. Abrecht, D. Ariosa, D. Cloëtta, D. Pavuna, L. Perfetti, M. Gioni, G. Margaritondo, *PHOTOEMISSION, CORRELATION AND SUPERCONDUCTIVITY: NEW AVENUES*, International Journal of Modern Physics B **17**, (18-20 II), 3449 (2003)

D. Ariosa, M. Abrecht, D. Cloëtta, D. Pavuna, M. Onellion, and G. Margaritondo, *Unexpected Electronic Properties of Strained* $La_{1.85}Sr_{0.15}CuO_4$ *Epitaxial Films*, IEEE TRANSACTIONS ON APPLIED SUPERCONDUCTIVITY **13** (2 III), 2733 (2003)

M. Abrecht, D. Ariosa, D. Cloetta, S. Mitrovic, M. Onellion, X. X. Xi, G. Margaritondo, D. Pavuna, *Strain and High Temperature Superconductivity: Unexpected Results from Direct Electronic Structure Measurements in Thin Films*, Physiscal Review Letters **91**, 057002 (2003)

M. Abrecht, D. Ariosa, D. Cloetta, S. Mitrovic, M. Onellion, X. X. Xi, G. Margaritondo, D. Pavuna, *Reply to Comment on ‘‘Strain and High Temperature Superconductivity: Unexpected Results from Direct Electronic Structure Measurements in Thin Films’’*, Physiscal Review Letters **92**, 129702 (2004)

M. Abrecht, D. Ariosa, D. Cloetta, D. Vobornik, G. Margaritondo, D. Pavuna, *Direct photoemission spectroscopy and electronic properties of in situ grown, strained high-*T_C *and related oxide films*, Journal of Physics and Chemistry of Solids **65** (8-9), 1391 (2004)

S. Mitrovic, P. Fazekas, C. Søndergaard, D. Ariosa, N. Barišić, H. Berger, D. Cloëtta, L. Forró, H. Höchst, I. Kupčić, D. Pavuna, G. Margaritondo, *Experimental Electronic Structure and Interband Nesting in* $BaVS_3$, http://xxx.lanl.gov/abs/cond-mat/0502144

D. Cloetta, D. Ariosa, M. Abrecht, C. Cancellieri, S. Mitrovic, M. Papagno, D. Pavuna, *Systematic Studies of* $La_{2-x}Sr_xCuO_4$ *in Direct Synchrotron Light: On the Role of Compressive against Tensile Strain*, Proc. SPIE Int. Soc. Opt. Eng. **5932**, 10 (2005)

This thesis is also on the internet: http://library.epfl.ch/theses/?nr=3333